

**Deanship of Graduate Studies  
Al-Quds University**



**Direct Measurements of the Magneto-Caloric Effect in Pulsed  
Magnetic Fields in Compounds of the Series  $Mn_{5-x}Fe_xSi_3$**

**Nour Abed Al-Majeed Maraytta**

**M.Sc. Thesis**

**Jerusalem – Palestine**

**1438/2017**

**Direct Measurements of the Magneto-Caloric Effect in Pulsed  
Magnetic Fields in Compounds of the Series  $Mn_{5-x}Fe_xSi_3$**

**Prepared By:**

**Nour Abed Al-Majeed Maraytta**

**B.Sc.: Physics Science, Al-Quds University, Palestine.**

**Supervisor:**

**Prof. Salman M. Salman**, Physics Department, Al-Quds University, Palestine

**Co-Supervisors:**

**PD Dr. Karen Friese**, Jülich Centre for Neutron Science-2, Forschungszentrum  
Jülich, Germany

**Dr. Jörg Voigt**, Jülich Centre for Neutron Science-2, FZ Jülich, Germany.

A thesis Submitted in Partial fulfillment of requirement for the degree of Master  
of Science from the Department of physics, Faculty of Science and Technology,  
Al-Quds University.

**1438/2017**



Deanship of Graduate Studies, Al-Quds University

## Thesis Approval

### Direct Measurements of the Magneto-Caloric Effect in Pulsed Magnetic Fields in Compounds of the Series $Mn_{5-x}Fe_xSi_3$

**Nour Abed Al-Majeed Maraytta**

Registration No: 21410822

#### Supervisors

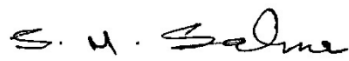
Prof. Salman M. Salman, Physics Department, Al-Quds University, Palestine.

PD Dr. Karen Friese, Jülich Centre for Neutron Science-2, FZ Jülich, Germany.

Dr. Jörg Voigt, Jülich Centre for Neutron Science-2, FZ Jülich, Germany.

#### Master thesis submitted and accepted.

#### Names and signatures of the examining committee members.

1. Head of the committee: Prof. Salman M Salman Signature: 
2. Internal Examiner: Prof. Elias I. Elias Signature: 
3. External Examiner: Prof. Mustafa Abu Safa Signature: 

Jerusalem – Palestine  
1438/2017

## **Dedication**

I lovingly dedicate this thesis to my parents for their endless love and being always proud of me.

To my sisters, brothers and friends for supporting me all the way,  
and to my little angel “Nour” who came and brought happiness with her.

**I owe you everything.**

**“And, when you want something, all the universe conspires in helping you to achieve it” ... Paulo Coelho, the Alchemist**

## Declaration

I, Nour Maraytta, declare that this thesis “**Direct Measurements of the Magnetocaloric Effect in Pulsed Magnetic Fields in Compounds of the Series  $Mn_{5-x}Fe_xSi_3$** ” and the work presented in it are my own and have been generated by me as the result of my own original research and that they have not been submitted earlier elsewhere.

I confirm that this work was done under the supervision of Prof. Salman M. Salman from the Physics Department, Al-Quds University, Palestine, and PD Dr. Karen Friese, Jülich Centre for Neutron Science-2, Forschungszentrum Jülich, Germany\*.

Nour Maraytta

Jerusalem – Palestine

1438/2017

---

\*This project is part of a collaborative effort under the framework collaboration between FZ-Jülich Research Center, Germany, and Al-Quds University, Palestine, and coordinated by Karen Friese, Jülich Centre for Neutron Science CNS-2 and Salman M. Salman from the Department of Physics and Director of Al-Quds Jülich Cooperation Program at Al-Quds University.



## Acknowledgments

At the beginning I want to thank **Allah** for giving me the strength and patience to complete this work. Of course, this work would not have been possible without the help of some people so it's a great pleasure for me to take this opportunity to thank them for standing with me to finish my thesis.

First, I would like to thank my advisor **Prof. Salman M. Salman** for his guidance during my university studies and providing the chance to conduct this experiment within the frame work of Alquds Jülich Cooperation.

I express my gratitude to **PD Dr. Karen Friese** for giving me the opportunity to work in her group and for her permanent interest in the progress of this work. I am indebted to her for her support, advice and endless patience she showed in improving my writing.

Special thanks to **Prof. Thomas Brückel** for providing support and hospitality to conduct my thesis at the wonderful JCNS-2.

I am deeply grateful to my scientific advisor **Dr. Jörg Voigt**, for his help in magnetization measurements, data analysis and in writing my thesis. He is always very patient in teaching me, his daily support and encouragement has been invaluable. Thanks to **Dr. Yurii Skourski** for his help in the measurements of the pulsed magnetic fields in Dresden High Magnetic Field Laboratory and his patience in teaching me the experimental skills.

Thanks to **DP. Jörg Persson** for his help in preparing the samples; to **Paul Hering, Mamuka Chikovani, Asma Qdemat, Sabreen Hammouda** and **Mohammed Ait Haddouch** for their help and support; thanks to Miss **Barbara Daegener** for her help in all administrative matters and special thanks to colleagues at JCNS-2 for their kindness. It has been a pleasure to be part of your institute.

Finally, I want to thank my family: **My Mom** for her true love and for supporting me in everything in my life, **my Dad** who I wish could have still been here today to share me these moments, to my grandmother for her love; to my brothers **Jad** and **Firas** whom I have always been able to depend on whenever I needed; to my youngest brother **Mohammed** for just being in my life, to all my sisters especially **Suha** and **Maha** for their incredible love and support at difficult times; and to my uncle **Osama** for his constant support. I am thankful to my friends especially **Israa, Haneen** and **Basel** for being so close even from the other side of the world. Ultimately, I am indebted to all my teachers and to all who stood by me in any way.

**Nour Maraytta**

## Abstract

The Magneto Caloric Effect (MCE) describes the change of temperature of a material when exposed to a magnetic field and forms the basis of magnetocaloric refrigeration technologies. This utilization of the effect can offer a novel method for cooling that is economically feasible and ecologically friendly. In addition it can save around 20-30% of the needed energy in comparison with traditional vapor compression technology, and hence the effect attracts the attention of many researches. MCE is identified by the temperature change ( $\Delta T_{ad}$ ) in an adiabatic process, and by the entropy change ( $\Delta S_{iso}$ ) in an isothermal process.

In the last years there has been an upsurge in the knowledge of the MCE and many materials have been investigated for their MCE characteristics. In the context of this project a single crystalline sample of the compositions  $Mn_{5-x}Fe_xSi_3$   $x=4$  was prepared in order to analyze the MCE in these materials. X-ray powder diffraction, using a Huber G670 diffractometer, shows that there are no indications of impurity phases. The Laue method was used to define the orientation of the single crystal samples for measurements of the magnetic properties. The samples were characterized with magnetization measurements using a PPMS and PPMS-Dynacool.

The magnetization measurements confirm earlier results and show that  $MnFe_4Si_3$  has a phase transition to a ferromagnetic ordered phase at approximately 300 K. A strong anisotropy of the magnetization and the magnetocaloric effect with the easy axis of magnetization in the a, b-plane is observed. The isothermal entropy change  $\Delta S$ , deduced from the hysteresis loops measured on single crystalline samples and derived on the basis of the Maxwell relation has a maximum of about 1.3 J/kgK for a field change of 1 T with an applied field along the a-axis, and a maximum of about 3.5 J/kgK for a field change of 6 T with an applied field along the c-axis.

The pulsed-field magnetization has been measured in fields up to 8 T, applying the field in [100] direction and up to 30 T with the field in [001] direction under nearly adiabatic conditions. The results obtained are in a good agreement with the data from steady-field isothermal measurements.

The adiabatic temperature change of  $MnFe_4Si_3$  single crystal sample was measured in the direction [100] in pulsed magnetic fields up to 50 T. For a field of 50 T an adiabatic temperature change of 9.45 K is observed at 320 K. For a field change of 20 T, a maximum adiabatic temperature change of 5.66 K is observed at 315 K, and for a field change of 2 T, a maximum adiabatic temperature change of 1.38 K is observed at the Curie temperature ( $T_C = 300$  K). For the measurements in [001] direction, a test pulse of 10 T was applied at 340 K, The data was not satisfactory due to imperfect mounted sample, and because of the limited magnet time available, measurements with the field applied in the [001] direction were therefore stopped.

# Contents

<b>Acknowledgments</b> .....	<b>ii</b>
<b>Abstract</b> .....	<b>iii</b>
<b>List of Tables</b> .....	<b>vi</b>
<b>List of Figures</b> .....	<b>vi</b>
<b>List of Abbreviations</b> .....	<b>ix</b>
<b>Introduction</b> .....	<b>1</b>
1.1 Motivation .....	1
1.2 Place of Research .....	2
<b>Theory</b> .....	<b>4</b>
2.1 The Magnetocaloric Effect (MCE).....	4
2.1.1 Background (Introduction and history) .....	4
2.1.2 Thermodynamics of Magnetocaloric Materials.....	7
2.1.3 Measurement of the magnetocaloric effect .....	9
2.1.3.1 Direct MCE measurements.....	9
2.1.3.2 Indirect measurements.....	11
2.2 Scattering theory and Diffraction Experiments .....	11
2.2.1 Introduction .....	11
2.2.2 Basics of x-ray diffraction on polycrystalline samples.....	12
2.2.3 The Le Bail method.....	13
2.3 Atomic and Magnetic Structure of $Mn_{5-x}Fe_xSi_3$ compounds .....	14
2.3.1 Crystal structure.....	14
2.3.2 Magnetic properties of $Mn_{5-x}Fe_xSi_3$ (Previous Studies).....	16
2.3.3 Why the system $Mn_{5-x}Fe_xSi_3$ is a good candidate for studies.....	17
<b>Experimental Setup and Techniques</b> .....	<b>18</b>
3.1 Sample Preparation.....	18
3.1.1 Synthesis of the polycrystalline samples of $Mn_{5-x}Fe_xSi_3$ with $x=4$ .....	18
3.1.2 Single crystal growth of $MnFe_4Si_3$ (Czochralski method).....	20
3.2 Scattering Techniques .....	22
3.2.1 X-ray powder diffraction experiment .....	23
3.2.2 Laue diffraction .....	24
3.3 Magnetization Measurements.....	25

3.3.1. Isothermal magnetization measurements in DC field.....	25
3.3.2 Adiabatic magnetization measurements in pulsed field .....	28
3.4 Direct Measurements of the MCE in a Pulsed Magnetic Field .....	31
<b>Data Analysis and Discussion .....</b>	<b>38</b>
4.1 Le Bail refinements of the powder diffraction data.....	37
4.2 Macroscopic Properties .....	38
4.2.1 Magnetization measurements .....	38
4.2.1.1 Magnetization measurements in DC field .....	38
4.2.1.2 Magnetization measurements in pulsed field .....	46
4.2.2 Direct measurements of the magnetocaloric effect in pulsed magnetic fields .....	47
<b>Conclusions and Future Work .....</b>	<b>54</b>
5.1 Conclusions .....	54
5.2 Future Work.....	55
<b>Bibliography.....</b>	<b>56</b>
<b>Appendix A .....</b>	<b>59</b>

## List of Tables

**Table 2.1:** The lattice parameters for the compounds of the series  $\text{Mn}_{5-x}\text{Fe}_x\text{Si}_3$ .

**Table 3.1:** The initial temperatures at which the pulses were applied in MCE measurements.

## List of Figures

### Chapter 1

**Figure 1.1:** Jülich Center for Neutron Science (JCNS).

**Figure 1.2:** Dresden High Magnetic Field Laboratory (HLD).

### Chapter 2

**Figure 2.1:** Schematic of a magnetic-refrigeration cycle.

**Figure 2.2:** The number of papers published annually containing the term 'magnetocaloric' in the title, over the past 50 years. The 2017 value is for the year first five month.

**Figure 2.3:** The S-T diagram illustrating the magnetocaloric effect.

**Figure 2.4:** Illustration of Bragg's law.

**Figure 2.5:** Two-dimensional powder diffraction setup with flat plate detector.

**Figure 2.6:** Flow chart of the Le Bail process.

**Figure 2.7:** Projection of the structure of  $\text{MnFe}_4\text{Si}_3$  in space group  $\text{P}\bar{6}$  at 380 K along the [001]-direction (left) and along the [120]-direction (right).

**Figure 2.8:** Magnetic phase diagram of the  $\text{Mn}_{5-x}\text{Fe}_x\text{Si}_3$  system ( $x=0,1,2,3,4,5$ ).

**Figure 2.9:** Schematic diagram illustrating the ferromagnetic structure of  $\text{MnFe}_4\text{Si}_3$  at 200 K in magnetic space group  $\text{Pm}'$ .

### Chapter 3

**Figure 3.1:** (A) Schematic drawing of an apparatus for cold crucible induction melting (B) Principle of cold crucible induction melting.

**Figure 3.2:** (A) Photo of the cold crucible induction melting apparatus used to prepare the samples; (B) Photo of the molten material in the crucible.

**Figure 3.3:** Schematic drawing of an experimental setup for single crystal growth using the Czochralski Method.

**Figure 3.4:** Photo showing the growth of the crystal and a picture of the final crystal.

**Figure 3.5:** (A) Schematic representation of a powder diffractometer with transmission geometry B) A photo of the diffractometer used in this work.

**Figure 3.6:** Photo of the sample used for the powder diffraction experiment.

**Figure 3.7:** (A) Photo of the MWL100 Camera System (B) the crystal fixed on the holder (C) a screenshot of the control software (D) an image from the Laue camera for the crystal of  $\text{MnFe}_4\text{Si}_3$  oriented along the c-axis.

**Figure 3.8:** (A) VSM option of the PPMS setup (B) a photo of the PPMS at JCNS-2.

**Figure 3.9:** Photos of the used sample for DC magnetization measurements on the sample holder.

**Figure 3.10:** Photo of one of the used samples for DC magnetization measurements mounted on the sample holder.

**Figure 3.11:** Magnetization measurements in pulsed magnetic field (A) The two samples, the holder and the tube (B) The samples after assembly.

**Figure 3.12:** The pickup-coil system used in the pulsed-field magnetometer with (left) the principal sketch, (middle) the electrical scheme, and (right) a photo of the original set up.

**Figure 3.13:** (A) Time dependences of the magnetic fields obtained with different pulsed magnets operational at the HLD (B) a photo of the used coil.

**Figure 3.14:** (a) Schematic drawing of the experimental set-up for MCE measurements in pulsed magnetic fields (b) Pictures of both sides of the sample holder together with the brass cylinder.

**Figure 3.15:** The experimental setup: (A) the four samples used in these measurements (B) a schematic drawing of the thermocouple (C) the holder with the samples mounted (D) the back side of the holder with the reference junction installed (E) the holder with the heater placed around the sample.

## Chapter 4

**Figure 4.1:** Observed, calculated and difference profile of  $\text{MnFe}_4\text{Si}_3$  measured at room temperature from the LeBail refinement.

**Figure 4.2:** Hysteresis loops of  $\text{MnFe}_4\text{Si}_3$  measured at temperatures from 20-350 K ( $H \parallel [100]$ ).

**Figure 4.3:** Hysteresis loop measured at 240 K with the linear function fitting ( $H \parallel [100]$ )

**Figure 4.4:** Bottom: magnetization in the saturation region; Middle: slopes in the saturation region; Top: slopes near zero field region.  $H \parallel [100]$ . Error bars are shown if they exceed the symbols size.

**Figure 4.5:** Hysteresis measured at temperatures from 60-380 K ( $H \parallel [001]$ ).

**Figure 4.6:** Hysteresis loop measured at 240 K with the linear function fitting ( $H \parallel [001]$ ).

**Figure 4.7:** Bottom: magnetization in the saturation region; Middle: slopes in the saturation region; Top: slopes near zero field region.  $H \parallel [001]$ . Error bars are shown if they exceed the symbols size.

**Figure 4.8:** Temperature-dependent magnetization of  $\text{MnFe}_4\text{Si}_3$  from hysteresis measurements ( $H \parallel [100]$ ).

**Figure 4.9:** Temperature-dependent magnetization of  $\text{MnFe}_4\text{Si}_3$  from hysteresis measurements ( $H \parallel [001]$ ).

**Figure 4.10:** MCE of  $\text{MnFe}_4\text{Si}_3$  calculated from the temperature-dependent magnetization at a field of 1 T ( $H \parallel [100]$ ).

**Figure 4.11:** MCE of  $\text{MnFe}_4\text{Si}_3$  calculated from the temperature-dependent magnetization at a field of 6 T ( $H \parallel [001]$ ).

**Figure 4.12:**  $M(H)$  curves in pulsed magnetic field and DC field at 5 K in  $[100]$  direction.

**Figure 4.13:**  $M(H)$  curves in pulsed magnetic field and DC field at 5 K with the field applied in  $[001]$  direction.

**Figure 4.14:** Comparison of  $\Delta T_{\text{ad}}$  for  $\text{MnFe}_4\text{Si}_3$  measured in pulsed magnetic fields of 2 T (black symbols), 20 T (red symbols) and 50 T (blue symbol).

**Figure 4.15:** field dependence of  $\Delta T_{\text{ad}}$  for different initial temperatures and a pulsed field change of (A, B) 2 T (C) 20 T (D) 50 T.

**Figure 4.16:** Time dependences of the adiabatic temperature change in pulsed magnetic field of 10 T at 340 K.

**Figure 4.17:** The time dependence of  $\Delta T_{\text{ad}}$  with pulsed fields of +10 T and -10 T at 340 K and the average of the two.

## Appendix

**Figure A1:** Part of the command sequence used in the magnetization measurements with  $H \parallel a$ -axis which was performed on PPMS-Dynacool.

**Figure A2:** Parts of the command sequence used in the last magnetization measurements in the direction ( $H \parallel c$ -axis) which were performed on the PPMS.

**Figure A3:** Python scripts which were used to plot the temperature-dependent magnetization curves of  $\text{MnFe}_4\text{Si}_3$  in  $H \parallel [100]$  and  $H \parallel [001]$  respectively.

## List of Abbreviations

MCE	Magnetocaloric effect
MCM	Magnetocaloric materials
P	Paramagnetic
F	Ferromagnetic
AF	Antiferromagnetic
H	Magnetic field strength
M	Magnetization
T	Absolute temperature
$T_C$	Curie Temperature
$S(T, H)$	Total entropy
$S_M$	Magnetic entropy
$S_L$	Lattice entropy
$S_E$	Electronic entropy
$\Delta S_{iso}$	Isothermal entropy change
$\Delta T_{ad}$	Adiabatic temperature change
XRD	X-ray diffraction
$\lambda$	Wavelength
D	Plane spacing
$wR_p$	Weighted profile R-factor
$R_p$	Profile R-factor
VSM	Vibrating Sample Magnetometer
PPMS	Physical Properties Measurement System
PEEK	Polyether ether ketone
HLD	The Dresden High Magnetic Field Laboratory
JCNS	Jülich Center for Neutron Science

## Introduction

---

### 1.1 Motivation

Room-temperature refrigeration for food storage and air conditioning is a necessary technology in our life and industries such as gaseous liquefaction. The gas compression/expansion refrigerators have been utilized everywhere since the first commercial refrigerator was successfully made [Zimm et al., 1998].

The increasing concerns about global warming as a result of the rising energy usage makes solving the issue of environmental pollution a demanding task for research today. Possible solutions include utilization ecologically friendly techniques; develop efficient ways for energy utilization.

The low efficiency of conventional vapor compression cooling techniques, in addition to their employment of the ozone-depleting chemicals (like chlorofluorocarbons (CFCs)), hazardous chemicals (as ammonia) and greenhouse gases (hydro chlorofluorocarbons (HCFCs), and hydro fluorocarbons (HFCs)) entails a high interest in replacing them by technologies that are energy-efficient and environmentally friendly [Tegus et al., 2002].

Magnetic refrigeration as a new solid state cooling technology at room-temperature, with a possible energy saving of 20%-30% could be an option for the refrigeration sector. The magnetocaloric cooling is an energy-efficient and environmentally friendly technology based on the Magneto Caloric Effect. The MCE is based on entropy changes of magnetic materials under an applied magnetic field, which leads to a change in the temperature of the material. Besides its practical application, MCE studies can give an extra insight into the nature of magnetic phase transitions.

The individual members of the series  $\text{Mn}_{5-x}\text{Fe}_x\text{Si}_3$  ( $x=0-5$ ) are known for their magnetocaloric properties. Magnetization measurements were used to study the magnetic phase transitions and the magnetocaloric properties of the individual compounds [Songlin et al., 2002]. Of particular interest of  $\text{MnFe}_4\text{Si}_3$  system, it has a transition from the paramagnetic to a ferromagnetic ordered state at around 300 K [Hering et al., 2015].

## 1.2 Place of Research

The experimental work presented in this thesis was done at the Forschungszentrum Jülich in Germany (GmbH), particularly at the Jülich Centre for Neutron Science (JCNS-2) (Figure 1.1) and at Helmholtz Zentrum Dresden Rossendorf (HZDR), particularly at Dresden High Magnetic Field Laboratory (HLD) (Figure 1.2).

**The Jülich Centre for Neutron Science (JCNS)** Forschungszentrum Jülich GmbH, was founded in 2006 to develop and operate neutron scattering instruments at several neutron sources worldwide. The in-house research focuses on correlated electron systems and nano-magnetism as well as soft matter and biophysics. Within these areas of expertise, the JCNS offers expert support at the neutron instruments including specialized sample environment and ancillary laboratory access for external users from science and industry.



**Figure 1.1: Jülich Center for Neutron Science (JCNS).**

The JCNS includes the divisions: Neutron scattering (ICS-1 / JCNS-1) and Scattering methods (PGI-4 / JCNS-2), and the newly founded institute JCNS-3 “Neutron Analytics for Energy Research. Related to the institute are several outstations at most important neutron sources worldwide (FRM II Garching, ILL Grenoble, and SNS 4 Oak Ridge).

**The Dresden High Magnetic Field Laboratory (HLD)** at the Helmholtz-Zentrum Dresden-Rossendorf (HZDR; established in 2004) focuses on modern materials research in high magnetic fields. In particular, electronic properties of metallic, semiconducting, superconducting, and magnetic materials are investigated. The High Magnetic Field Laboratory serves as a research facility for both in-house and user projects and provides research opportunities for pulsed magnetic fields up to 90 T for routine operation. So far, they operate four magnets (A, B, D, and E).



**Figure 1.2: Dresden High Magnetic Field Laboratory (HLD)**

## **2.1 The Magnetocaloric Effect (MCE)**

### **2.1.1 Background (Introduction and history)**

The study of magnetic refrigeration started with the discovery of MCE 120 years ago. The MCE leads to a temperature change of a material due to the application or removal of a magnetic field [Yu et al., 2003]. Currently, there is a high interest in utilizing the MCE as an alternative technology for refrigeration, in particular for application close to room temperature. In addition, the magnetocaloric effect is frequently employed to reach very low temperatures ( $< 20$  K) [Pecharsky and Gschneidner, 1999].

Magnetic refrigeration is expected to have great potential for applications due to a series of reasons. First, it does not employ ozone-depleting chemicals, hazardous chemicals, or greenhouse gases as refrigeration media. Secondly, electromagnets, superconductors or permanent magnets, could be used in the magnetic refrigeration with no need for compressors that have portable components at large rotational speed resulting in mechanical vibration, noise, poor stability and brief life. Finally, magnetic refrigerators working with Gd can yield a cooling efficiency of 60% of the theoretical limit, in comparison to just about 40% in the perfect gas-compression refrigerators. A reduced consumption of fossil fuels and CO<sub>2</sub> production will be the good news of using magnetic refrigerators with high efficiency [Tegus et al., 2002].

Figure 2.1 shows a schematic of a magnetic-refrigeration cycle. Yellow and green colors show the magnetic material in low and high magnetic fields, respectively.

The application of the magnetic field aligns the randomly oriented magnetic moments reducing the magnetic entropy. In return the lattice entropy is increased and the magnetic material heats up. When the heat is removed by a heat-transfer medium and the magnetic

field is turned off, the magnetic moments randomize again, increasing the magnetic entropy. This in turn results in a decrease of the lattice entropy or a cooling of the magnetic material below the ambient temperature. Based on the operating temperature, the heat-transfer medium could be water (with antifreeze) or air for ordinary cooling, and helium or hydrogen for low temperatures [Brück, 2005].

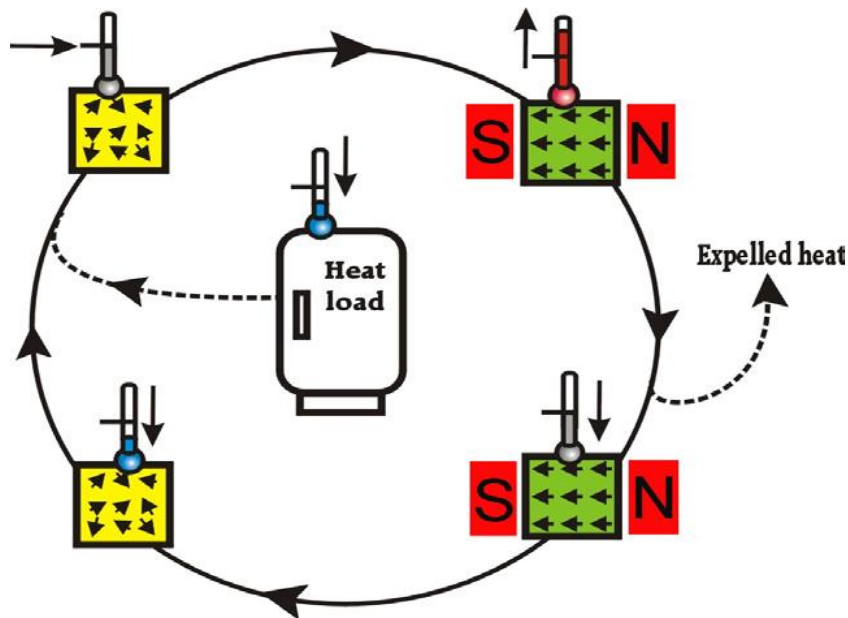


Figure 2.1: Schematic of a magnetic-refrigeration cycle [Brück, 2005].

The interest in the MCE has been triggered by Brown's work near room temperature magnetic refrigerator [Brown,1976; Brown, 1978] and the discovery of the large MCE near room temperature in  $Gd_5Si_2Ge_2$  [Pecharsky and Gschneidner, 1997]. The effect has been extensively studied for many magnetic materials after those revolutionary works [Oliveira and Ranke, 2010].

### History of the MCE

In 1881 the thermal effect of metal iron was discovered by Warburg when he was testing it under a varying magnetic field. The nature of the MCE was explained by Debye [Debye, 1926] and Giauque [Giauque, 1927] who suggested independently the possibility of reaching ultralow temperatures (lower than of liquid helium) in the adiabatic demagnetization. The method was successfully verified by [Giauque and MacDougall, 1933] and the first adiabatic demagnetization refrigerator that reached 0.25 K was experimentally demonstrated.

Giauque was awarded the Nobel Prize in physics for his work on magnetic refrigeration in 1949 [Yu et al., 2003].

Advances in utilization of the MCE for cooling occurred between 1933 and 1997. Brown designed the first magnetic refrigerator working at room temperature in 1976. About 15 years later, Green et al. [Green et al., 1990] built a device that was able to cool a load besides the magnetocaloric material itself and the heat exchange fluid [Gschneidner et al., 2008].

The year 1997 witnessed two major millstones: The first on February 20, 1997 delivered the proof that room temperatures magnetic refrigeration is viable and competitive with possible energy savings of around 30% [Zimm et al., 1998]. The second event was on June 1997 when the Giant MCE (GMCE) was discovered in  $Gd_5(Si_2Ge_2)$  [Gschneidner et al., 2005].

In 2001 at Astronautics Corporation, the first “room-temperature magnetic refrigerator” using permanent magnets was built. Many other designs followed afterwards. The current research is focused on the discovery of novel magnetocaloric materials, as the magnitude of MCE in the magnetic materials is the key to a high cooling capacity. In addition, the availability of suitable permanent magnets, and the overall design of the device is in the focus of attention [Gschneidner et al., 2008].

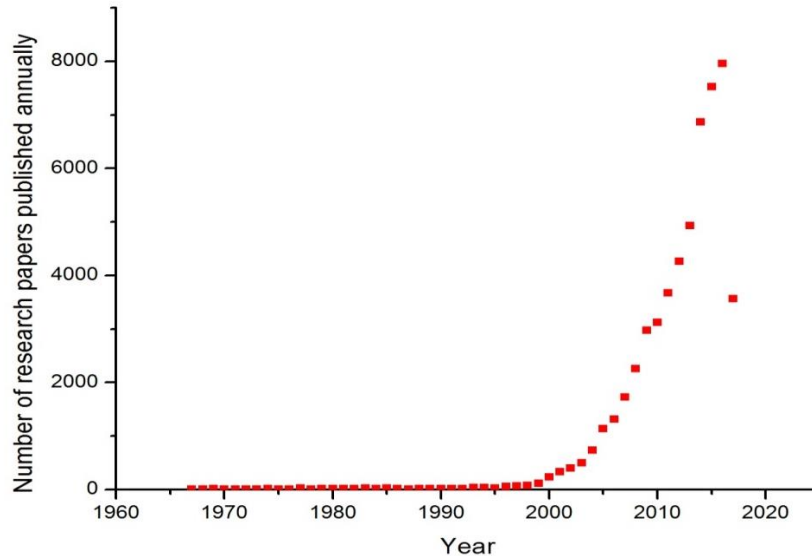


Figure 2.2: The number of papers published annually containing the term 'magnetocaloric' in their title over the past 50years. The 2017 value is for the year first five month [WEB OF SCIENCE].

## 2.1.2 Thermodynamics of Magnetocaloric Materials

The total entropy at constant pressure  $S(T, H)$  is a function of the magnetic field strength ( $H$ ) and absolute temperature ( $T$ ). It is composed of three parts: magnetic entropy ( $S_M$ ), lattice entropy ( $S_L$ ), and electronic entropy ( $S_E$ ) as shown in equation (1)

$$S(T, H) = S_M(T, H) + S_{Lat}(T) + S_{EI}(T) \quad (1)$$

$S_M$  is a function of  $H$  and  $T$ , yet  $S_{Lat}$  and  $S_{EI}$  are functions of  $T$  only, which means that a change in the strength of the magnetic field only changes the magnetic entropy  $S_M$ . The MCE results from the coupling of the magnetic sub lattice with the magnetic field. This is an intrinsic property of all magnetic materials. If the field is applied isothermally, the magnetic entropy of the paramagnetic or soft ferromagnetic materials decrease, they eject heat. Conversely, if the field is lowered isothermally the system will absorb heat and the magnetic entropy increases [Yu et al., 2003].

The thermodynamics of the MCE in ferromagnetic materials near the Curie temperature is illustrated in Figure 2.3. It shows the behavior of the total entropy  $S(T)$  of a ferromagnetic material vs. temperature under zero and non-zero magnetic fields. The solid lines represent the total entropy for two values of the magnetic field:  $H_0=0$  and  $H_1>H_0$ . The dotted line shows the non-magnetic entropy (lattice and electronic), and the dashed lines show the behavior of the magnetic entropy for the two fields.

When the magnetic field is applied in a reversible adiabatic process the total entropy stays constant. The adiabatic temperature increase  $\Delta T_{ad} = T_1 - T_0$  represents the difference between the relevant  $S(T)_H$  functions as shown by the horizontal arrow in Figure 2.3. Alternatively, if the magnetic field is applied isothermally, the MCE can be expressed in terms of the magnetic entropy reduction  $\Delta S_M = S_1 - S_0$ . This representation is equivalent to the isothermal difference between the  $S(T)_H$  functions and shown by the vertical arrow in Figure 2.3.  $\Delta T_{ad}$  and  $\Delta S_M$  represent the two characteristic values of the MCE. Both depend on the initial temperature  $T_0$  before the application of the magnetic field, and the field difference  $\Delta H = (H_1 - H_0)$  [Pecharsky and Gschneidner, 1999].

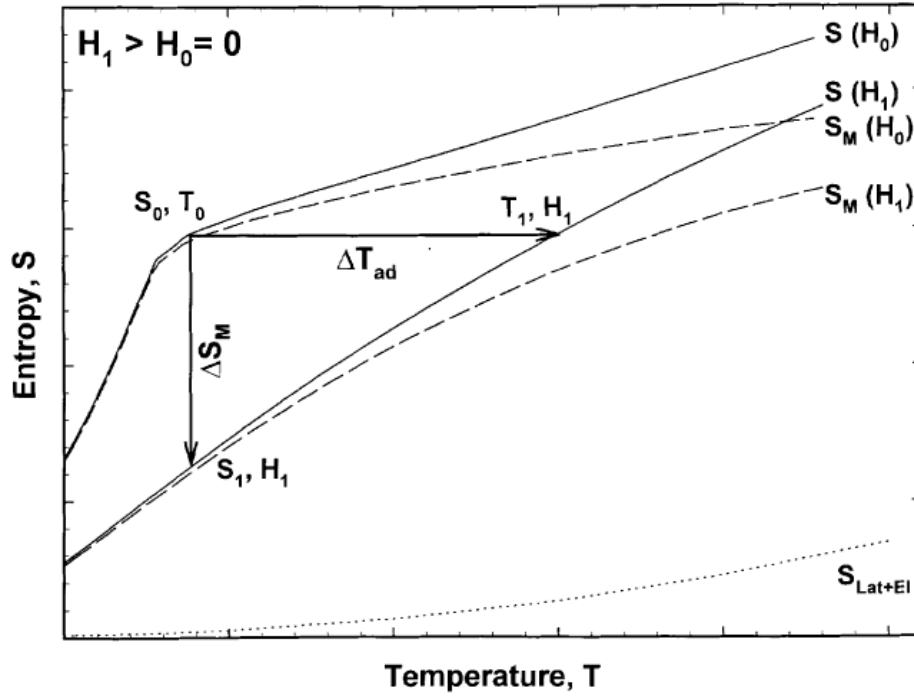


Figure 2.3: The S-T diagram illustrating the magneto caloric effect [Pecharsky and Gschneidner, 1999].

Maxwell's relations can be used to calculate  $\Delta T_{ad}$  and  $\Delta S_M$  [Morrish, 1965]:

$$\left(\frac{\partial S(T,H)}{\partial H}\right)_T = \left(\frac{\partial M(T,H)}{\partial T}\right)_H \quad (2)$$

Where, H is the magnetic field, M is the magnetization, and S is the entropy. Integration for an isothermal-isobaric process yields:

$$\Delta S_M(T, \Delta H) = \int_{H_1}^{H_2} \left(\frac{\partial M(T,H)}{\partial T}\right)_H dH \quad (3)$$

This equation states that the magnetic entropy change is proportional to the derivative of magnetization with respect to temperature at constant field and to the magnetic field change. For adiabatic processes, the infinitesimal adiabatic temperature rise is obtained from combining equation (2) and TdS equation (with  $C dT = dQ$  and  $dQ = -T dS$ ) which gives:

$$dT = - \left(\frac{T}{C(T,H)}\right)_M \left(\frac{\partial M(T,H)}{\partial T}\right)_H dH \quad (4)$$

From this equation it follows that the adiabatic temperature rise is inversely proportional to the heat capacity, while it is directly proportional to the absolute temperature; the derivative

of magnetization with respect to temperature at constant field; and to the magnetic field change. By integrating Eq. (4) we get the indicator for the size of the MCE:

$$\Delta T_{\text{ad}}(T, \Delta H) = - \int_{H_1}^{H_2} \left( \frac{T}{C(T,H)} \right)_M \left( \frac{\partial M(T,H)}{\partial T} \right)_H dH \quad (5)$$

These four equations play an essential role in understanding the behavior of the magnetocaloric effect in solids and looking for new materials with a large MCE. One should emphasize the following points [Pecharsky and Gschneidner, 1999]:

- $\Delta S_M(T)_{\Delta H}$  is negative (Eqs.(2), (3)), while  $\Delta T_{\text{ad}}(T)_{\Delta H}$  is positive (Eqs. (4), (5)) which is apparent from Figure 2.3. This is because the magnetization of paramagnets and simple Ferromagnets at constant field decreases with increasing temperature [ $(\partial M/\partial T)_H < 0$ ].
- From equations (2) and (3) it follows that in Ferromagnets  $|(\partial M/\partial T)_H|$  is maximum at  $T_C$ , and therefore,  $|\Delta S_M(T)_{\Delta H}|$  must have a peak at  $T_C$ .
- $\Delta T_{\text{ad}}(T)_{\Delta H}$  in Ferromagnets shows a peak at  $T_C$  when  $\Delta H \rightarrow 0$ . This behavior is similar to what happens in  $\Delta S_M(T)_{\Delta H}$  (Both values gradually reduce above and below  $T_C$ ).

### 2.1.3 Measurement of the magnetocaloric effect

The MCE can be measured directly or calculated indirectly. The direct method gives access to the adiabatic temperature change ( $\Delta T_{\text{ad}}$ ). The indirect experiments can provide  $\Delta T_{\text{ad}}(T)_{\Delta H}$  from heat capacity measurements and  $\Delta S_M(T)_{\Delta H}$  from magnetization measurements.

#### 2.1.3.1 Direct MCE measurements

Direct methods always include the measurement of the initial  $T_0$  and final  $T_F$  temperatures of the sample, when an external magnetic field is changed adiabatically from  $H_0$  to  $H_F$ . The adiabatic temperature change is equal to

$$\Delta T_{\text{ad}}(T_0, H_F - H_0) = T_F - T_0 \quad (6)$$

Direct MCE measurements can be performed by using contact and non-contact techniques, depending on whether the temperature's sensor is in direct thermal contact with the sample or not. Contact techniques are suitable for large temperature changes and strong magnetic fields

[Dan'kov et al., 1997; Gopal et al., 1997], while non-contact techniques are suitable for small changes in temperature and weak magnetic fields. The latter techniques are based on the thermo-acoustic principle in which a sample with a periodically changing surface temperature induces exponentially decaying pressure waves, which can be detected by a sensitive microphone [Pecharsky and Gschneidner, 1999].

A fast change of the magnetic field is required to ensure adiabatic conditions. The field can be varied by moving the sample or the magnet, [Dan'kov et al., 1997; Gopal et al., 1997]. In this case, permanent or superconducting magnets are usually used, with a magnetic field range of 0.1-10 T, and for the electromagnets the field operates at less than 2 T [Pecharsky and Gschneidner, 1999].

A better alternative is to alter the field by using pulsed fields while leaving the sample and the magnet unmoved [Dan'kov et al., 1997; Gopal et al., 1997]. Direct MCE measurements from under 1 to 40 Tesla using this method have been reported.

If one takes into account all possible error sources, the experimental accuracy of the direct methods is within 5-10%. Factors influencing the accuracy include errors in thermometry and in the field setting, the quality of the sample thermal insulation, the quality of the compensation scheme to eliminate the effect of the ultrafast magnetic field change (dB/dt contributions) on the temperature sensor reading and any other factors [Dan'kov et al., 1997; Gopal et al., 1997; Pecharsky and Gschneidner, 1999].

In addition to giving the adiabatic temperature change ( $\Delta T_{ad}$ ) directly which is an essential parameter for magnetic refrigeration, direct measurements are closer to the real process used in applications. The pulse lengths of the nondestructive pulsed-field facilities are in the range 10-100 ms and that agree with the targeted operation frequency of the magnetic refrigerators, 10-100 Hz [Kuz'min, 2007].

A direct MCE measurement in pulsed magnetic fields provides the opportunity to examine the dynamics of the MCE in the suitable frequency range. Furthermore, the accessible magnetic field range is extended to beyond 70 T and the short pulse duration provides nearly adiabatic conditions during the measurement [Zavareh, 2016].

### 2.1.3.2 Indirect measurements

Indirect experiments estimate both  $\Delta T_{ad}(T, \Delta H)$  and  $\Delta S_M(T, \Delta H)$  from heat capacity measurements, or  $\Delta S_M(T, \Delta H)$  from magnetization measured as a function of temperature and magnetic field after a numerical integration of equation (3), and both methods show reasonable agreement with each other. Most of the MCE studies are based on magnetization measurements and the calculated  $\Delta S_M(T)$ . The accuracy of  $\Delta S_M(T, \Delta H)$  from magnetization data depends on the accuracy of the magnetic moment, temperature, and field measurements. Because of the substitution of the exact differentials ( $dM$ ,  $dH$  and  $dT$ ) by the measured variations ( $\Delta M$ ,  $\Delta T$  and  $\Delta H$ ), the error in  $\Delta S_M(T, \Delta H)$  is reported to be within 3-10%, which makes the method popular [Foldeaki et al., 1995; Pecharsky and Gschneidner, 1999].

In this thesis, the MCE has been measured directly in pulsed magnetic fields up to 50 T using a contact technique (a thermocouple glued to the sample surface) and indirectly from magnetization measurements in DC fields up to 8.5 T. The techniques are described in Chapter 3.

## 2.2 Scattering Theory and Diffraction Experiments

### 2.2.1 Introduction

Scattering is a method used for obtaining structural information on a material. Diffraction effects can occur when a beam of electromagnetic radiation is scattered by a periodic structure with a repeat distance similar to the wavelength of the radiation. X-rays are a suitable probe for diffraction in crystalline materials as they have wavelengths not exceeding a few angstroms, and this is the typical interatomic distance in crystalline solids ( $\approx 0.15\text{--}0.4$  nm). Constructive interference happens when the X-rays diffracted by different parallel lattice planes are in phase. If they are out of phase, destructive interference occurs and there is no reaction [Birkholz, 2006]. The occurrence of constructive interference is explained by Bragg's law given by:

$$2d_{hkl} \sin \theta = n\lambda$$

Where  $d_{hkl}$  is the spacing between parallel lattice planes with Miller indices  $(hkl)$ ,  $\theta$  is the angle between the lattice planes,  $\lambda$  is the wavelength of the x-rays and  $n$  is an integer number. From this equation, it follows that for a fixed wavelength  $\lambda$ , and values of  $\theta$  and  $d$  satisfying the above equation, intensity maxima occur due to constructive interference of the scattered beam. Each observed peak in an X-ray diffraction diagram thus represents a certain set of parallel lattice plane  $(h k l)$ .

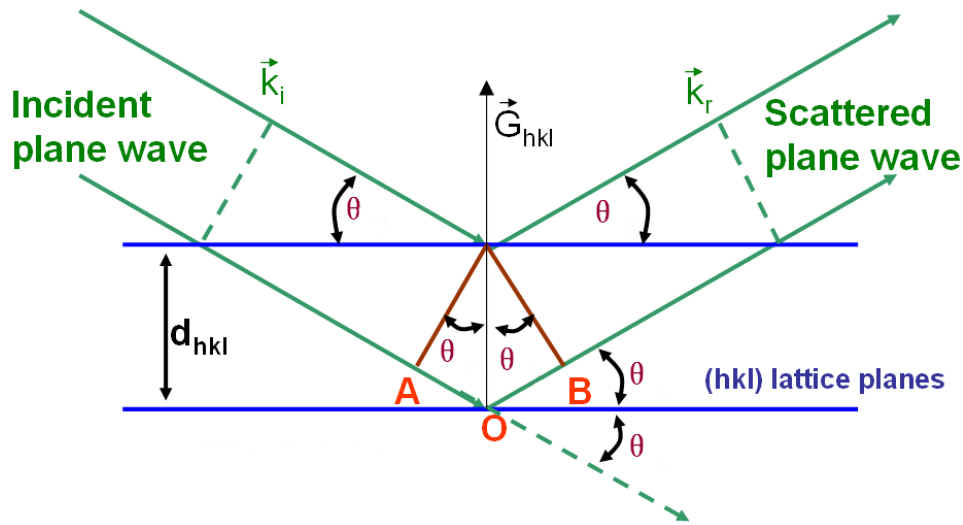


Figure 2.4: Illustration of Bragg's law [Cheng, 2014].

In this thesis X-ray powder diffraction was employed to check the phase purity, and Laue diffraction was used to determine the orientation of the measured crystal.

### 2.2.2 Basics of x-ray diffraction on polycrystalline samples

X-ray powder diffraction is a common technique mainly used for phase identification of a crystalline material and provides information on atomic spacing. The term powder means that the crystallites are randomly oriented in the sample so the powder can be seen as a polycrystalline material in which all possible orientations of a crystal lattice exist ideally in equal proportions.

In a powder diffraction experiment, a monochromatic X-ray beam is directed toward a sample consisting of many small randomly oriented crystals and it is scattered by the

electrons of the atoms inside the crystal. When Bragg's Law is fulfilled and constructive interference occurs concentric cones emanate from the sample position as shown in (Figure 2.5). These will then appear as a series of concentric rings on a detector placed normal to the X-ray beam. The 2-dimensional diffraction images can then be integrated to produce a one-dimensional plot of intensity against diffraction angle ( $2\theta$ ) with discrete peaks occurring at all scattering angles that satisfy the Bragg's condition.

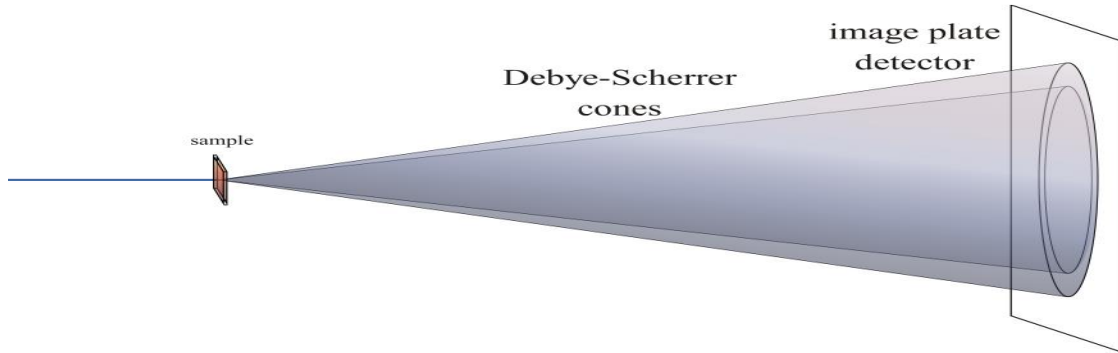


**Figure 2.5: Two-dimensional powder diffraction setup with flat plate detector** [<http://en.wikipedia.org>].

Laue diffraction is used for the determination of crystal orientation. This method is different from powder diffraction as it uses a polychromatic “white” ray beam comprising a range of wavelengths, which means that a fixed crystal is irradiated with a wide range of wavelengths. The incident angle  $\theta$  is fixed and each crystal plane (hkl) has a specific orientation with respect to the incoming beam. When a specific wavelength satisfies Bragg's condition, constructive interference for the scattered beams of a set of parallel lattice planes can occur and a diffraction spot can then be recorded on the detector. This implies that each spot corresponds to a set of parallel lattice planes (hkl) and a particular wavelength [**Cullity and Stock, 1956**].

### **2.2.3 The Le Bail method**

The Le Bail method [**Le Bail et al., 1988**] determines the unit cell parameter and possible space groups of a crystalline compound. During the refinement, many parameters can be fitted simultaneously such as: the zero shift, background parameters and the parameters that describe the shape of the observed peaks (profile function). Many programs are available that perform refinement of powder data using Le Bail refinement. For this thesis, the program Jana 2006 [**Petricek et al., 2006**] was used.

These following steps are executed in a Le Bail refinement (Figure 2.6): starting from the initial cell parameters, the diffraction diagram is calculated and compared with the observed data, then the difference is minimized at each point in the diagram by adjusting the parameters of background, lattice and profile function. After this, a new diffraction diagram is calculated and again compared with the observed data. This is repeated until a good agreement between the two diagrams is satisfied. The so-called R-factors are used determine the fit quality. The two most important are:

Weighted profile R-factor: 
$$wR_p = \sqrt{\frac{\sum \omega(y_{obs} - y_{calc})^2}{\sum \omega y_{obs}^2}} \%$$

Profile R-factor: 
$$R_p = \frac{y_{calc} - y_{obs}}{y_{calc}}$$

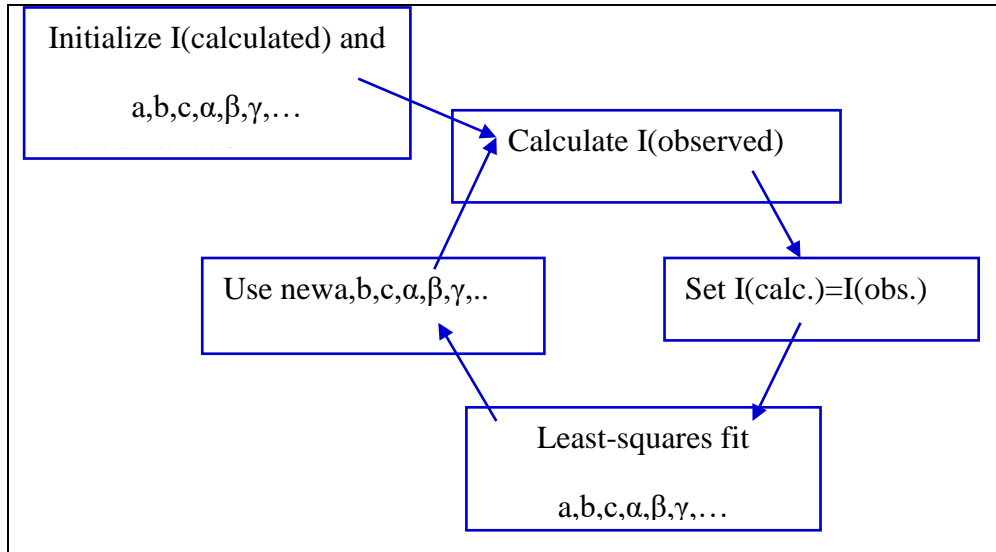


Figure 2.6: Flow chart of the Le Bail process.

## 2.3 Atomic and Magnetic Structure of $Mn_{5-x}Fe_xSi_3$ compounds

### 2.3.1 Crystal structure

The compounds in the series  $Mn_{5-x}Fe_xSi_3$  exhibit magnetocaloric effects at various temperatures depending on the x values. All compounds of the series possess a hexagonal symmetry at 293 K and 77 K. They crystallize in space group  $P6_3/mcm$  [Binczycka et al., 1973]. Two sites M1 (Wyckoff position 6g) and M2 (Wyckoff position 4d) are filled by Mn and Fe with various ratios based on the parameter x. It was found that most of the Mn atoms

are incorporated into the M1 site, while the M2 site is preferentially occupied by Fe atom [Johnson et al., 1972]. Atoms on the M1 site are interconnected to form distorted octahedra which share common triangular faces and form chains of composition  $\infty[(M1)_3]$  along the c-direction. The M2 site is surrounded by six silicon atoms at distances of approximately 2.4 Å in the form of a distorted octahedron. These octahedra share triangular faces with neighboring octahedra  $[M2Si_6]$  and form infinite chains of composition  $\infty[(M2)Si_3]$  along the c-direction [Binczycka et al., 1973; Gourdon et al., 2014]. Table 2.1 shows the lattice parameters for the compounds of the series  $Mn_{5-x}Fe_xSi_3$  at room temperature as published in [Binczycka et al., 1973].

**Table 2.1: The lattice parameters for the compounds of the series  $Mn_{5-x}Fe_xSi_3$**

x	$a_0(\text{Å})$	$c_0(\text{Å})$	$v_0(\text{Å}^3)$
0	$6.9077 \pm 0.00004$	$4.8131 \pm 0.00004$	198.90
1	$6.8849 \pm 0.00009$	$4.7861 \pm 0.00008$	196.49
2	$6.8538 \pm 0.00005$	$4.7579 \pm 0.00005$	193.56
3	$6.8301 \pm 0.00004$	$4.7390 \pm 0.00004$	191.46
4	$6.8054 \pm 0.00007$	$4.7290 \pm 0.00005$	189.68

Of particular interest is  $MnFe_4Si_3$  system, which has lattice parameters of  $a = 6.80572(22)$  Å and  $c = 4.72965(16)$  Å at 300 K. By using x-ray and neutron single crystal diffraction refinements, a new structural model in space group  $P\bar{6}$  was found, in which Mn and Fe atoms occupy one of the transition metal sites (M1a, M1b) in a partially ordered manner, while the other transition metal site (M2a, M2b) is completely filled by Fe atoms.

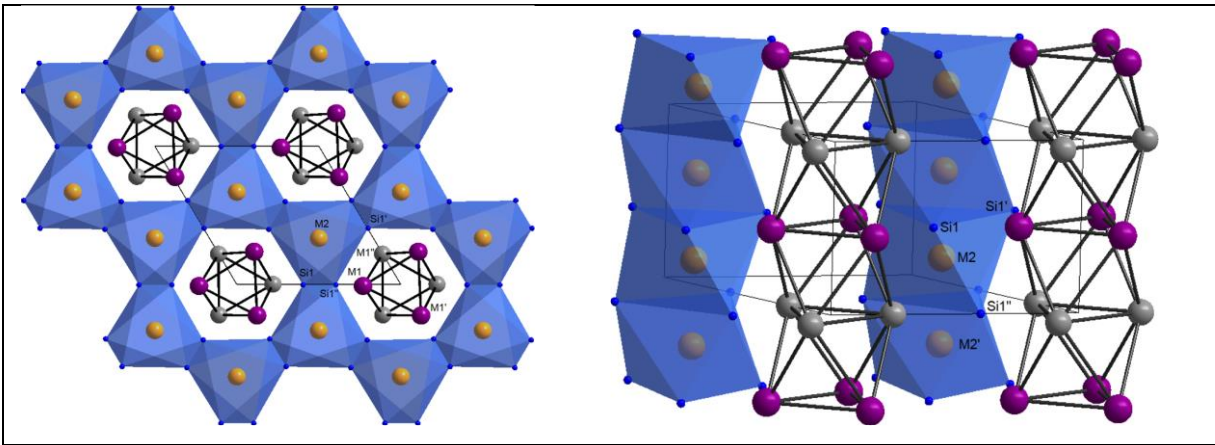


**Figure 2.7: Projection of the structure of  $MnFe_4Si_3$  in space group  $P\bar{6}$  at 380 K along the  $[001]$ -direction (left) and along the  $[120]$ -direction (right) [Hering et al., 2015].**

Figure 2.7 shows the projection of the structure of  $\text{MnFe}_4\text{Si}_3$  in space group  $\text{P}\bar{6}$  at 380 K along the [001]-direction (left) and along the [120]-direction (right). Sites occupied by Mn and Fe are shown in magenta (M1a) and gray (M1b); sites exclusively occupied by Fe are shown in orange; Si atoms are shown in blue, shortest distances between M1a and M1b sites are indicated in black, and  $[\text{FeSi}_6]$ - octahedra are indicated in blue [Hering et al., 2015].

### 2.3.2 Magnetic properties of $\text{Mn}_{5-x}\text{Fe}_x\text{Si}_3$ (Previous Studies)

Depending on the stoichiometry, the compounds in the system  $\text{Mn}_{5-x}\text{Fe}_x\text{Si}_3$  ( $x = 0, 1, \dots, 5$ ) undergo various magnetic phase transitions at different temperatures. The magnetic transitions have been investigated by magnetization measurements as a function of temperature on polycrystalline samples and the magnetic transition temperatures are shown in Figure 2.8. Two different antiferromagnetic phases are observed for the Mn-rich compounds ( $x = 0, 1, 2, 3$ ). The paramagnetic phase P transforms to a antiferromagnetic structure AF2. At lower temperatures a second to an antiferromagnetic structure AF1 occurs in all 4 compounds. On the other hand, for the Fe-rich compounds only a Ferromagnetic ordered phase F is observed [Songlin et al., 2002; Binczycka et al., 1973].

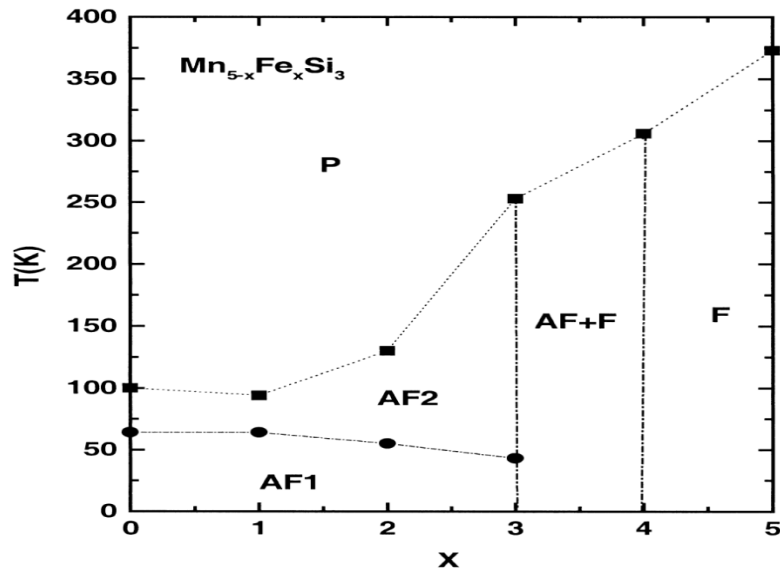


Figure 2.8: Magnetic phase diagram of the  $\text{Mn}_{5-x}\text{Fe}_x\text{Si}_3$  system ( $x=0,1,2,3,4,5$ ) [Songlin et al., 2002].

The compound  $\text{MnFe}_4\text{Si}_3$  which is studied in this thesis has a phase transition to a Ferromagnetic ordered phase at approximately 300 K [Hering et al., 2015; Gourdon et al., 2014]. A refinement of the magnetic structure based on neutron data measured on a  $\text{MnFe}_4\text{Si}_3$  single crystal in the magnetic space group  $\text{Pm}'$  confirms that this compound has a

strong anisotropy of the magnetization (and consequently of the magnetocaloric effect) with the easy axis of magnetization in the a,b-plane. It was shown that the spins on the sites with mixed occupancy of Mn and Fe are aligned in the a,b-plane, but it was not possible to refine a significant magnetic moment for the site exclusively occupied by iron (Figure 2.9) [Hering et al., 2015]. This is in clear contrast to the earlier results obtained from Rietveld refinements performed in the magnetic space group  $P6_3/mc'm'$  on polycrystalline material, which assumed that the magnetic spins order parallel to the [001]-direction [Gourdon et al., 2014].

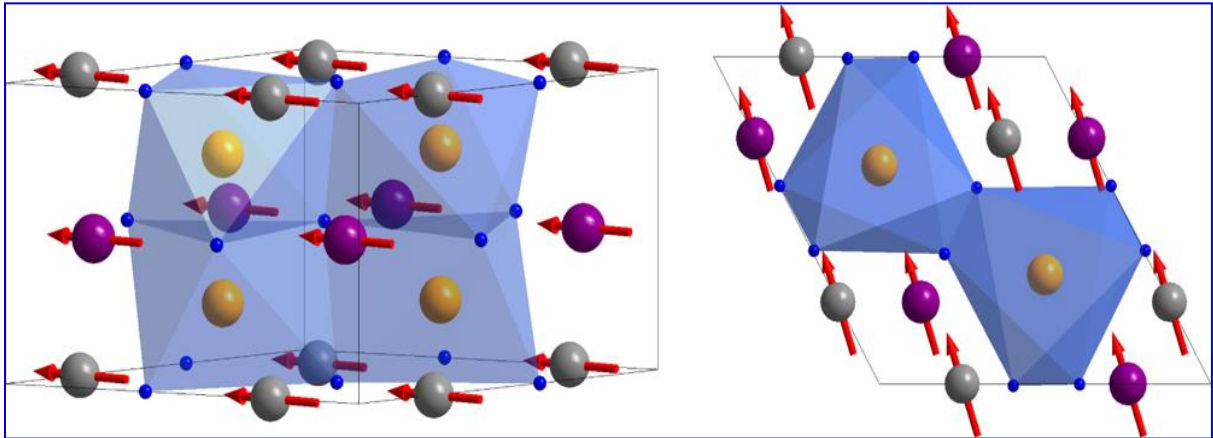


Figure 2.9: Schematic diagram illustrating the ferromagnetic structure of  $MnFe_4Si_3$  at 200 K in magnetic space group  $Pm'$ . Left, slightly tilted projection approximately along [110]-direction; right, projection along [001]- direction [Hering et al., 2015].

With the field applied along the a-axis, the magnetic entropy change deduced from the hysteresis loops measured on single crystal samples using the Maxwell relation has a maximum of  $-2.90$  J/kgK for a field change of 2 T [Hering et al., 2015] which is slightly higher than the values observed for polycrystalline samples ( $\approx -2$  J/kgK at a field change from 0 to 2 T and  $\approx -4$  J/kgK for a field change from 0 to 5 T [Gourdon et al., 2014; Songlin et al., 2002]. With the field applied along the c-axis, the entropy change is considerably smaller (approx.  $-1.3$  J/kgK) [Hering et al., 2015].

### 2.3.3 Why the system $Mn_{5-x}Fe_xSi_3$ is a good candidate for studies

Even though the MCE in these materials is moderate, the materials could potentially perform well after some optimization through doping. In addition, they are made up of low-cost, abundant and non-toxic elements and they are less brittle compared to competing materials. Moreover, it is possible to synthesize these materials as large single crystal, which is

impossible for the majority of other magnetocaloric materials (MCM) that are commonly available in polycrystalline form. This offers a major advantage for obtaining knowledge about the basic mechanism of the MCE because the availability of large single crystals enables to apply a series of experimental techniques not available for polycrystalline samples.

# 3

## Experimental Setup and Techniques

---

### 3.1 Sample Preparation

#### 3.1.1 Synthesis of the polycrystalline samples of $\text{Mn}_{5-x}\text{Fe}_x\text{Si}_3$ with $x=4$

Polycrystalline ingots of  $\text{MnFe}_4\text{Si}_3$  were prepared using stoichiometric amounts of the elements using cold crucible induction melting under argon atmosphere.

For a method a water cooled structure is used which is surrounded by induction coils [Stefanovsky et al., 2016]. The sample is placed in a crucible and heated by an electric field generated in it from high frequency alternating current (AC) that passes through the multi-turn induction coils surrounding the glass tube that covers the copper crucible. The process is performed in vacuum for high purity of the final material.

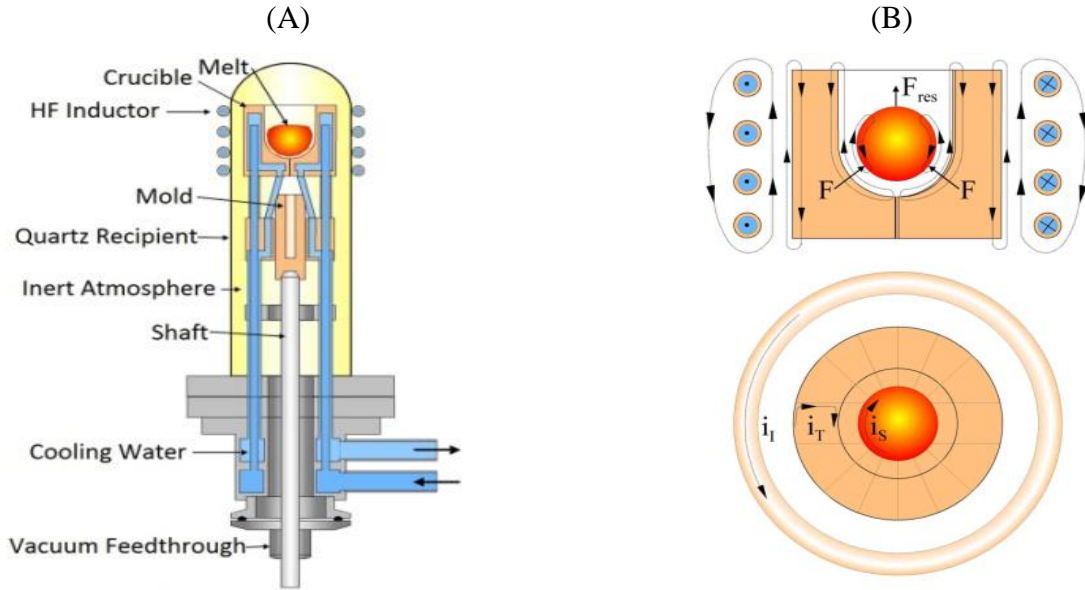


**Figure 3.1:** (A) Schematic of an apparatus for cold crucible induction melting (B) Principle of cold crucible induction melting [Beyss and Gier, 2014].

Figure 3.1(A) shows a schematic of a cold crucible induction melting apparatus, and Figure 3.1(B) illustrates the principle. The crucible is divided into many segments; each is insulated from the next one and connected to a water pipe for cooling. The induced current  $I_T$  cycles in each segment and that generates an induced current  $I_S$  in the sample and as a result the required magnetic field. When the power is increased, eddy currents cause joule heating that melts the metal. The Lorentz forces, minimize the thermal losses, accelerate the process of further heating, and start to partially levitate the charges. Additional forces  $F$  generated from the interaction between the induced currents and the magnetic field, result in further movements in the melt. In this way, a melt of high homogeneity and purity grades can be produced by performing constant and well controlled stirring.

For the synthesis of  $MnFe_4Si_3$  polycrystalline samples, constituent elements, manganese, iron and silicon were weighed and mixed in stoichiometric ratios. The materials were put in a copper crucible with the larger pieces down and smaller up to prevent them from falling out. All raw materials were heated under vacuum to remove any existing impurities from the surface until they started to glow, and the pressure of the sample's chamber was stabilized. After this, they were melted with high frequency alternating magnetic fields in argon

atmosphere and quenched to room temperature. Figure 3.2 shows the used apparatus and the melting process.

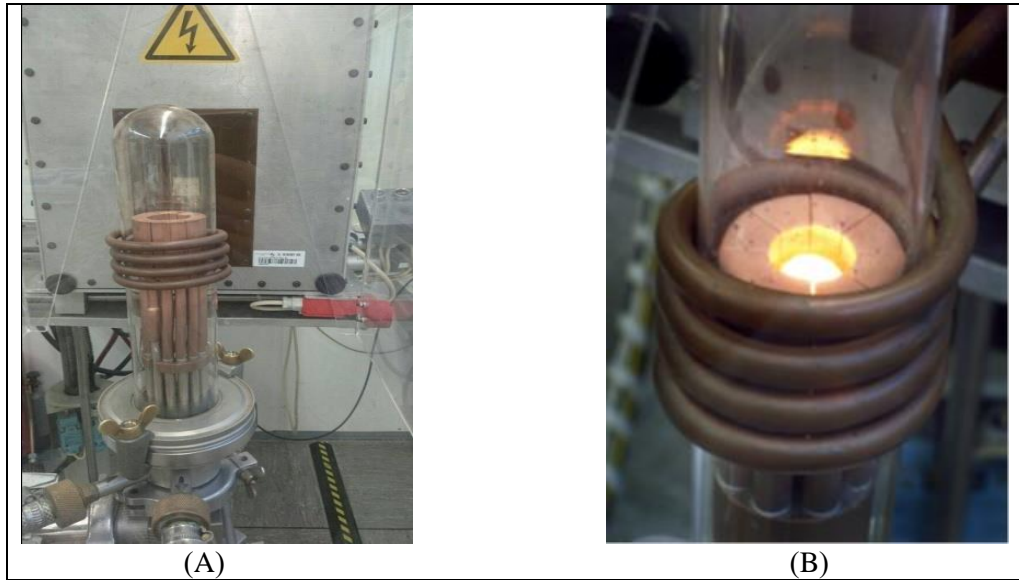


**Figure 3.2: (A) Photo of the cold crucible induction melting apparatus used to prepare the samples; (B) Photo of the molten material in the crucible. Photo B from [Cheng, 2014].**

The operation was repeated two times. Each time the sample was turned around to ensure a high homogeneity of the melt. The obtained polycrystalline sample was cleaned mechanically at the surface to remove any contamination. This polycrystalline material was then used as starting materials for the growth of a large single crystal.

### **3.1.2 Single crystal growth of $\text{MnFe}_4\text{Si}_3$ (Czochralski method)**

A large single crystal of  $\text{MnFe}_4\text{Si}_3$  was grown from the polycrystalline material by the Czochralski method in an aluminum oxide crucible using tungsten crystals as seed crystals. The method is used for large single crystal growth in an inert atmosphere [Czochralski, 1918]. Figure 3.3 illustrates the setup.

At the beginning of the growth procedure, polycrystalline pieces are filled in a crucible of a suitable material with a diameter larger than the one needed for the single crystal. This crucible is then inserted into another crucible which stands on a holder with copper coils surrounding it. For heating the sample, an alternating current passes through the coils and

heats the solid in the crucible due to its electrical conductivity until the polycrystalline pieces in the crucible melted down.

The rod with the tungsten seed crystals is lowered into the melt and at the interface between the seed and the melt the single crystal starts to grow while the rod is moved upwards with a specific speed. During this process the rod is rotating so that the resulting single crystal will have a cylindrical shape. The diameter of the single crystal can be controlled by controlling some factors such as the pulling and rotation speed and the power used for heating the crucible.

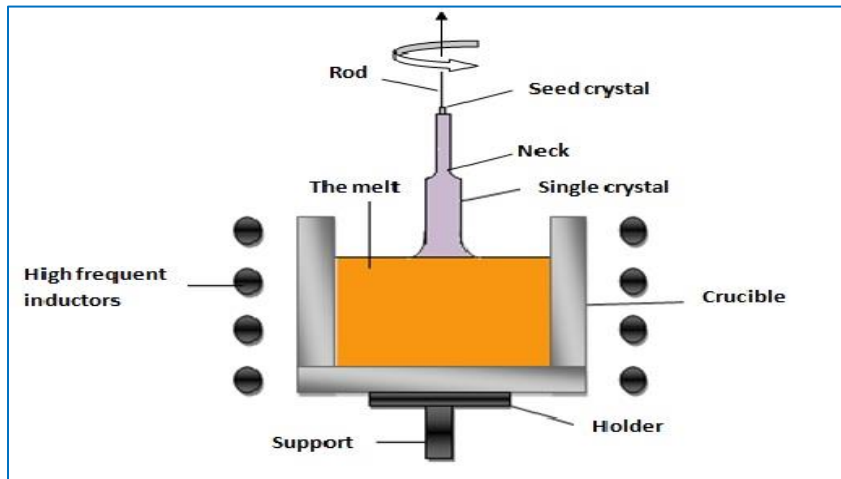


**Figure 3.3: Schematic drawing of an experimental setup for single crystal growth using the Czochralski Method.**

For the synthesis of  $\text{MnFe}_4\text{Si}_3$  83 g of polycrystalline material were filled into an aluminum oxide crucible, which was cleaned with ethanol prior to filling. The aluminum oxide crucible was inserted into a larger ceramic crucible and then put at the center of the furnace crucible to ensure that the heat was evenly distributed.

After closing the system, the power supply was switched on and the samples were heated up in vacuum. After melting the material in argon atmosphere, the single crystal growth started with the seed crystal of tungsten mounted on a rod of 3 mm diameter, also made of tungsten. The necking method was used to obtain a crystal of good quality. In this method the diameter of the crystal is reduced at the beginning of the synthesis to remove undesired grains and dislocations. Once a single grain was obtained, the diameter was enlarged.

The rod was then moved upwards with a speed of 10 mm/h and a rotation speed of 20 rev/m (Figure 3.4, left). The changing in the diameter of the crystal between the neck and the rest of it was controlled by the heating power and therefore by the melt temperature. The final single crystal had a diameter of about 10 mm. Unfortunately, due to internal stress the neck of the crystal broke before taking it out of the crucible (Figure 3.4, right).



**Figure 3.4: Photo showing the growth of the crystal and a picture of the final crystal.**

Some small pieces of the broken material were grounded further for x-ray powder diffraction experiment to check the quality of the sample. The larger part of the crystal was checked and oriented with a Laue camera. Spark erosion was used to cut four equal samples (5mm×5mm×1mm) for pulsed field measurements, two of them with the shortest dimension in [100]-direction and the other two with the shortest dimension in [001]-direction. Pieces of remaining parts of the crystal were used for magnetization measurements in DC field.

### **3.2 Scattering Techniques**

**The Huber G670 powder diffractometer:** Figure 3.5 shows a schematic view of the used Guinier geometry powder diffractometer. The diffractometer is equipped with a Cu X-ray tube. With the help of a monochromator the Cu- $K_{\alpha}$  radiation (1.54 Å) is selected. To improve the divergence of the beam soller slits is introduced between the monochromator and the

sample. The diffractometer has an integrated imaging plate detector with which the data can be acquired in a few minutes and only a small amount of the sample (several mg) is needed for the measurements.

Inside the detector housing, there is a laser recording unit with photomultiplier and pre-amplifier to read out the imaging plate. A halogen lamp is used to reset the information on the imaging plate after exposure and read out. The diffraction signal is stored as intensity data versus  $2\theta$  by the control software.

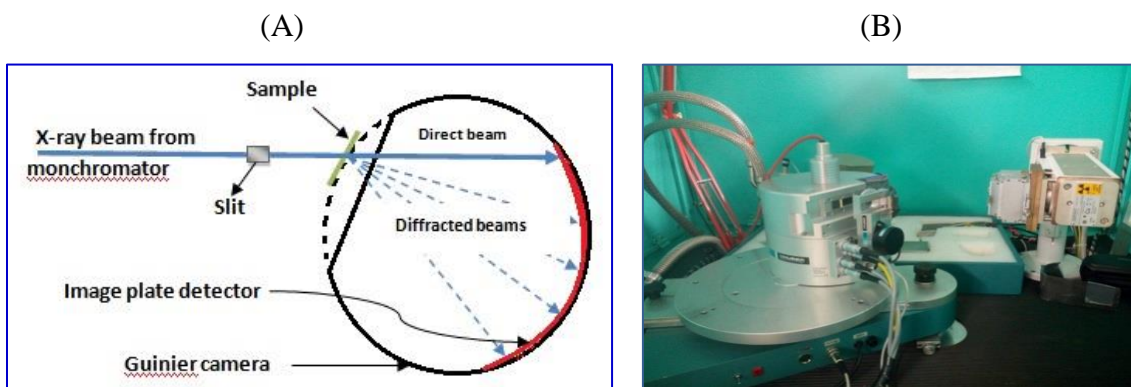


**Figure 3.5: (A) Schematic representation of a powder diffractometer with transmission geometry (B) A photo of the diffractometer used in this work.**

### 3.2.1 X-ray powder diffraction experiment

For the powder diffraction experiments a few milligrams of the sample were crushed in a mortar to obtain a very fine powder. After cleaning the sample holder, a piece of cellophane foil (Mylar-thin film) was used. The foil is visible in the powder diffraction diagram as a small increase in the background in the small angle area.

A very small amount of the sample was put on the middle of the foil together with a few drops of isopropanol. The sample was then mixed with the isopropanol and distributed homogeneously until a smooth flat surface was obtained. The mixture was left to dry and then covered with another piece of foil.

The two foils were fixed together with a metal ring and mounted in a Huber G670 X-ray powder diffractometer (Figure 3.6). Measurements were carried out at room temperature in

transmission geometry using Cu-K $\alpha$  radiation (1.54 Å). The sample was exposed for 240 minutes. To obtain a better statistics the sample oscillated during exposure with a frequency of about 1 Hz and amplitude of 10 mm.



**Figure 3.6: Photo of the sample used for the powder diffraction experiment.**

### **3.2.2 Laue diffraction**

Laue diffraction was used to check the larger segment of the synthesized single crystal. Two differently oriented grains were found within the segment and their locations were specified. Spark erosion was used to separate them and later on the same fraction was used to prepare all other samples.

A Multi wire MWL100 Real-Time Back-Reflection Laue Camera System (MWL100 Camera System; Figure 3.7 A) was used to define the orientation of the crystals by viewing the back reflection images on a computer screen in real time.

The crystal was mounted on a rotatable holder (Figure 3.7 B), then the holder with the crystal was installed in the instrument. The Orient Express software (Figure 3.7 C) was used to simulate the Laue pattern and the crystal was rotated until the desired orientation was obtained (Figure 3.7 D).

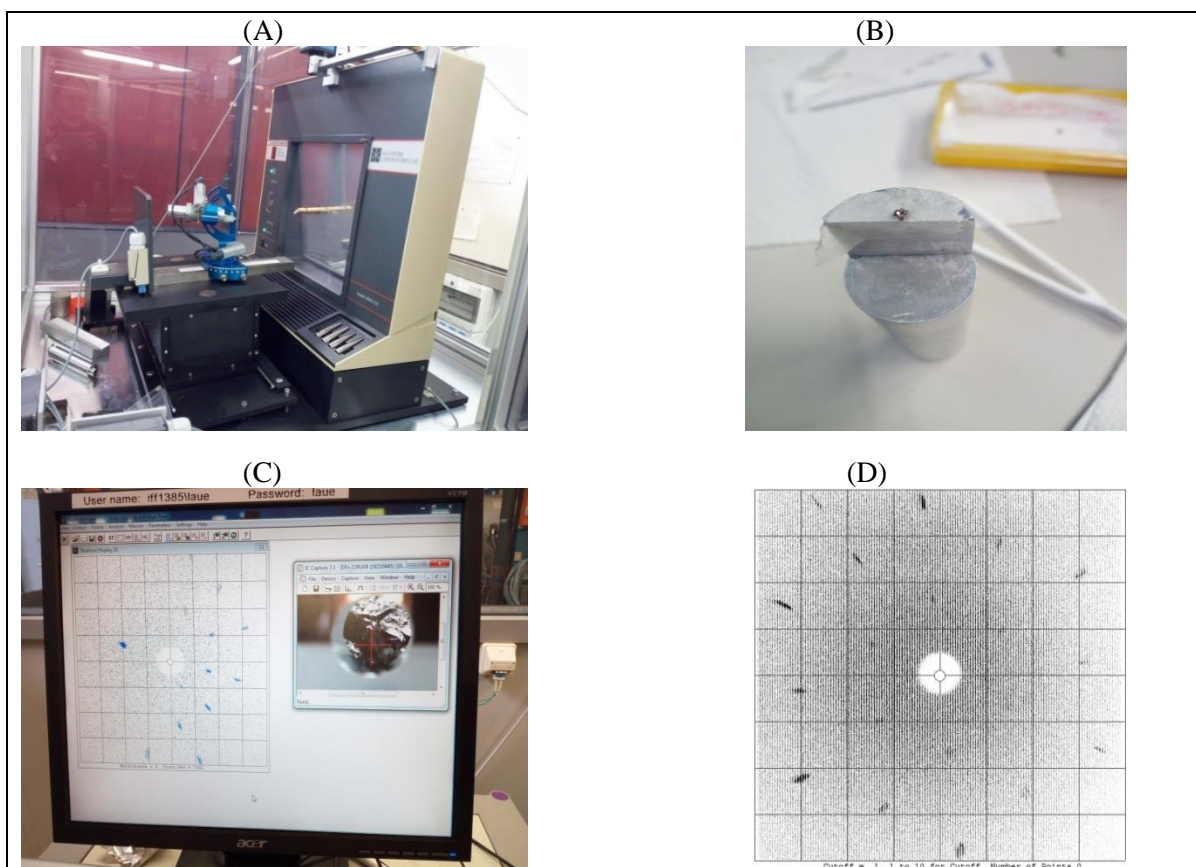


**Figure 3.7:** (A) Photo of the MWL100 Camera System (B) the crystal fixed on the holder (C) a screenshot of the control software (D) an image from the Laue camera for the crystal of  $\text{MnFe}_4\text{Si}_3$  oriented along the  $c$ -axis.

### 3.3 Magnetization Measurements

In this work two kinds of magnetization measurements were done on  $\text{MnFe}_4\text{Si}_3$ , the first one in DC field, which were carried out in the Jülich Center for Neutron Science (JCNS-2) and the other in pulsed field which were performed in Dresden High Magnetic Field Laboratory (HLD) at the Helmholtz-Zentrum Dresden-Rossendorf (HZDR).

#### 3.3.1. Isothermal magnetization measurements in a DC field

Direction dependent magnetization measurements  $M(H)$  on  $\text{MnFe}_4\text{Si}_3$  single crystals in DC fields have been performed by using a vibrating sample magnetometer (VSM) manufactured

by Quantum Design System PPMS and PPMS Dynacool. Measurements were made with the magnetic field directed parallel to the crystallographic a-axis then with the field parallel to c-axis.

### Quantum Design: Physical Property Measurement System (PPMS)

PPMS can perform magnetic, thermal and electrical measurements using various options designed for it (in this work, VSM option was used). In our system the field can reach 9 T, the temperature can go down to 1.9 K, and the magnetization can be measured with a sensitivity of  $10^{-6}$  emu.

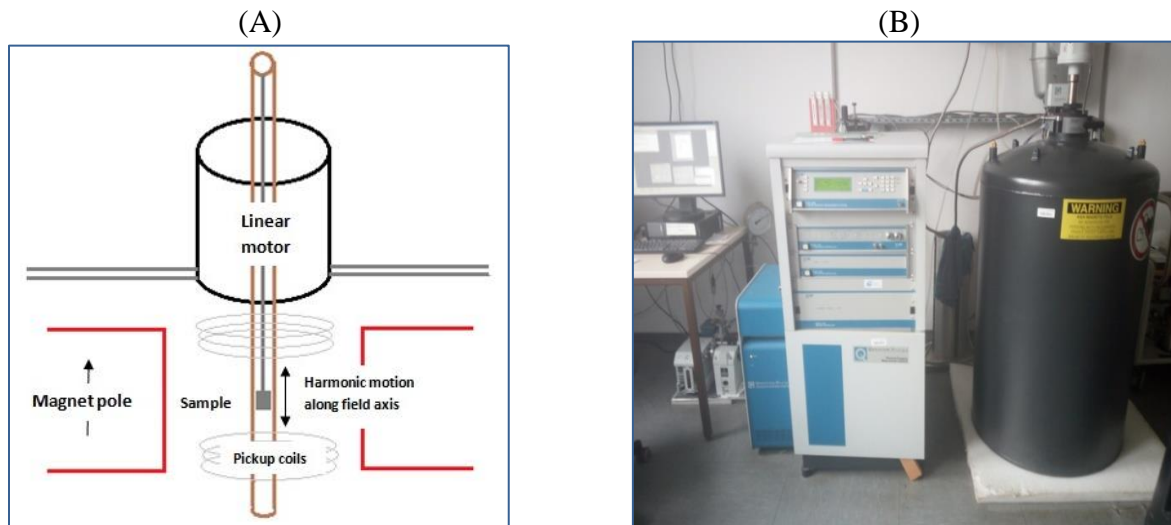


**Figure 3.8: (A) VSM option of the PPMS setup (B) a photo of the PPMS at JCMS-2.**

The VSM option operation is based on Faraday's law of induction. The sample oscillates inside inductive pick-up coils under the influence of a linear motor. The vibrating sample causes a change in the magnetic flux of the pickup coils, inducing a voltage in them that is proportional to the sample's magnetic moment. Figure 3.8 (A) shows a schematic of a typical VSM and Figure 3.8 (B) shows a photo of the PPMS used in JCMS-2.

The PPMS Dynacool, uses the same principle, a comparable magnetic field (9 T) and a lower temperature of 1.4 K can be reached compared QM PPMS (1.9 K). The main difference between the two designs is that QM PPMS uses an external supply of liquid cryogenics for

cooling while PPMS Dynacool has a water cooled He-compressor (closed-cycle), which expands He in a pulse tube cold head and liquefies a small amount of He for magnet and sample cooling [**Dynacool user's manual**].



**Figure 3.9: Photos of the used sample on the sample holder**

First, magnetization measurements with  $H \parallel a$ -axis were performed using PPMS-Dynacool. A small sample (18.3 mg) of  $MnFe_4Si_3$  was used, checked with the Laue camera to define the orientation and then mounted with a small amount of GE varnish on the sample holder (Figure 3.9 left).

Special care was taken to mount the sample at the correct location on the holder, to ensure the correct position inside the pickup coil. The holder with the sample was left under a lamp for at least half hour until the varnish dried and then it was covered with Teflon (Figure 3.9, right). The holder with the sample on it was inserted in the Dynacool.

A scan for the sample position in the magnetic field within the Dynacool was done using a small field of 100 Oe to ensure the sample was in the right place (center of magnetic field). A file containing the sequence of the measurements was created to define the procedure. Hysteresis loop measurements ( $M(H)$ ) were carried out in a field from -1 to 1 T with a sweep rate of 50 Oe/sec in the temperature range from 20 to 350 K with 10 K increase in each step (see appendix, Figure A1).

After that, magnetization measurements in the other direction ( $H \parallel c$ -axis) were performed on the QM PPMS. A sample of 5.8 mg was used and mounted on the holder the same way as mentioned before. Hysteresis loop measurements ( $M(H)$ ) were carried out under a field from 6 to 0.5 T (starting from 6 T at each temperature so that the sample was always saturated at the beginning of the measurement) with a sweep rate of 198 Oe/sec, then from 0.5 to -0.1 T

with a sweep rate of 20 Oe/sec in a temperature range from 60 to 260 K with 20 K increase in each step, then from 260 to 340 K with a 2 K increase and from 340 to 380 K with 10 K steps (Appendix, Figure A2). Figure 3.10 shows a photo of the last sample mounted on the holder. At the end, two hysteresis loops were performed at low-temperature (5 K) to calibrate the pulsed field measurements, one of them with the field parallel to the a-axis using sample of 7.5 mg and the other with the field parallel to c-axis using a 5.8 mg sample.



**Figure 3.10: Photo of one of the used samples mounted on the sample holder.**

For the  $H \parallel a$ -axis measurement, the field was changed from 8 to 0.5 T with a sweep rate of 198 Oe/sec, then from 0.5 to -0.5 T with a sweep rate of 20 Oe/sec and finally from -0.5 to -8 T with a sweep rate of 198 Oe/sec. A similar procedure was applied for ( $H \parallel c$ -axis) measurement but with 8.5 T instead of 8 T.

### **3.3.2 Adiabatic magnetization measurements in pulsed field**

For the first time, adiabatic magnetization measurements in pulsed fields were performed on  $\text{MnFe}_4\text{Si}_3$  by using the induction method. As mentioned before, these measurements were carried out in Dresden High Magnetic Field Laboratory (HLD).

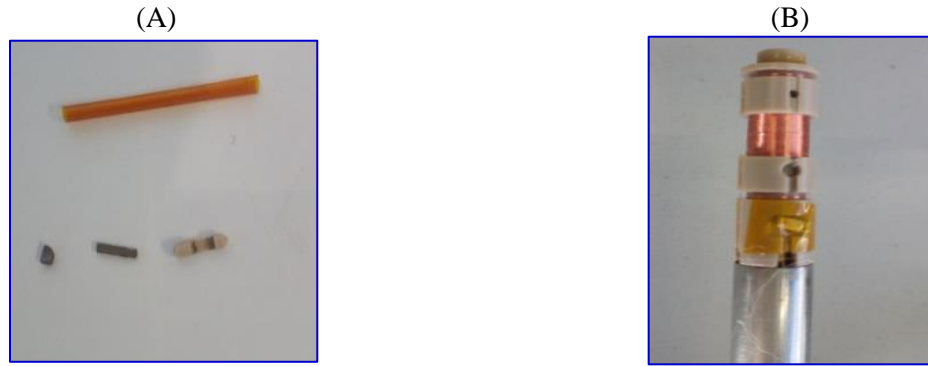


**Figure 3.11: Magnetization measurements in pulsed magnetic field (A) A photo of the two samples, the holder and the tube (B) The samples after assembly.**

For these measurements, two small samples were used; the first one (7.3 mg) was cut in a way that when it is mounted, the magnetic field will be parallel to the c-axis and the second one (14.3 mg) was cut in a way that the field is parallel to the a-axis.

For the measurements, the sample was mounted in a very small holder, then the holder with the sample on it was entered into a tiny tube and installed at the center of a pickup coil (Figure 3.11). The coil is 4 mm long and consists of 2000 turns of 40  $\mu\text{m}$  copper wire convoluted around the sample space which has 2 mm in diameter.

Figure 3.12 shows the pickup-coil system used in the pulsed-field magnetometer with (left) the principal sketch, (middle) the electrical scheme, and (right) the actual set up. For measuring the magnetization by the pickup coil in a varying magnetic field, this coil must be connected to another coil to cancel the influence of induction  $dH/dt$ . Many arrangements are possible for the compensated pickup coil system. The coaxial geometry was selected because it is the least sensitive to the field gradient and vibrations. The compensation coil was wound around a support of 6.8 mm in diameter. The residual uncompensated part, which is caused by the temperature-dependent contribution, is reduced at each temperature by a fine-compensation circuit using another additional coil [Figure 3.12; Skourski et al., 2011].

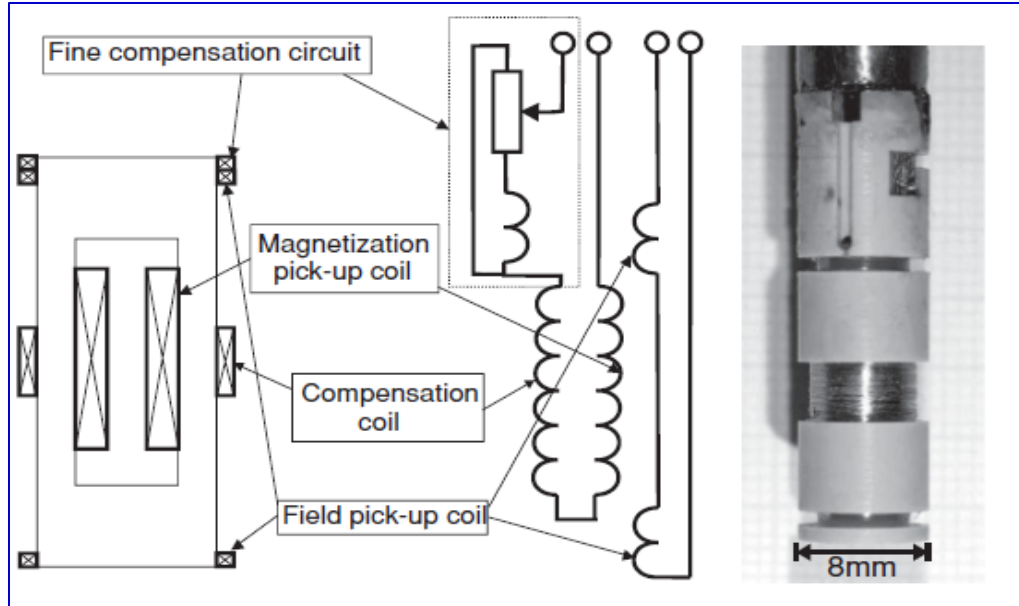


**Figure 3.12: The pickup-coil system used in the pulsed-field magnetometer with (left) the principal sketch, (middle) the electrical scheme, and (right) a photo of the original set up [Skourski et al., 2011].**

For measuring the magnetic field, two pick-up coils were used connected in series, and located at equal distance below and above the magnetization pick-up coil and sufficiently far (about 10 mm) to prevent the effect of the sample on the field measurement. The coil's signal which is proportional to  $dH/dt$  was stored using a digitizer and later integrated numerically. The well-known magnetization curve of  $MnF_2$  which displays a temperature-independent spin-flop transition at 9.27 T was measured to calibrate the pick-up coil signal [Skourski et al., 2011].

The magnetization measurement for each sample involved measurements of the signal from the pick-up coil with the sample in it at the desired temperature, and the background (signal without the sample) under the same conditions. The sample's magnetization was then found by subtracting the background from the first signal [Skourski et al., 2011]. For the easy direction, the magnetization measurement was carried out in pulsed magnetic fields up to 8 T and for the c axis (hard direction), the magnetization was performed in pulsed fields up to 30 T. Both measurements were done at a temperature of 4.2 K.

### 3.4 Direct Measurements of the MCE in a Pulsed Magnetic Field

The direct measurements of the MCE were also performed at Dresden High Magnetic Field Laboratory (HLD) by using home-built experimental set-ups (Figure 3.14). Three major components are required: the magnetic field, a cryostat for cooling or heating the sample (Helium-4 ( $^4\text{He}$ )) and a suitable thermometer for measuring the sample's temperature.

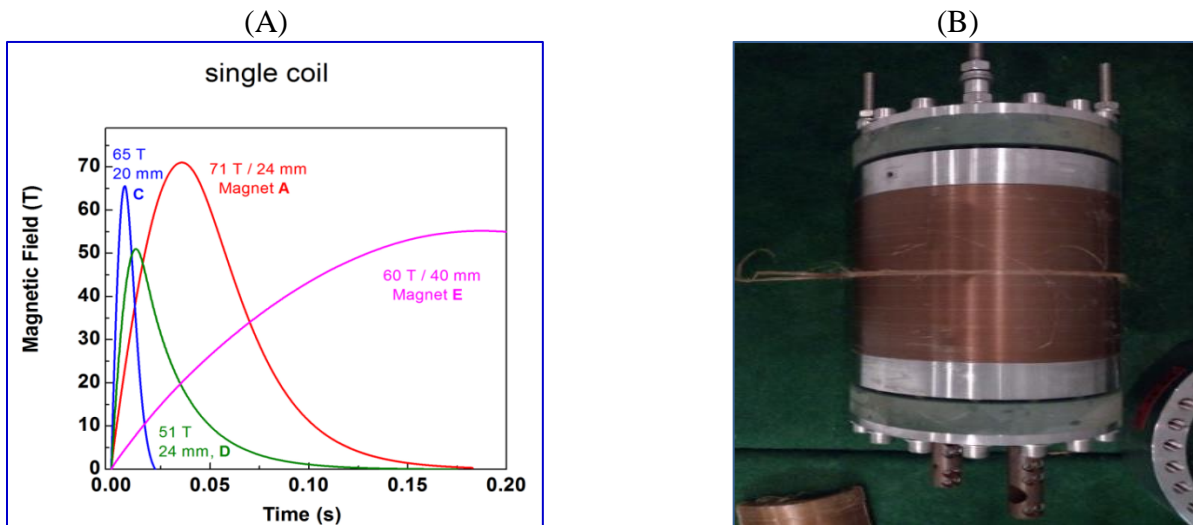


Figure 3.13: (A) Time dependences of the magnetic fields obtained with different pulsed magnets operational at the HLD [Zherlitsyn et al., 2012] (B) a photo of the used coil.

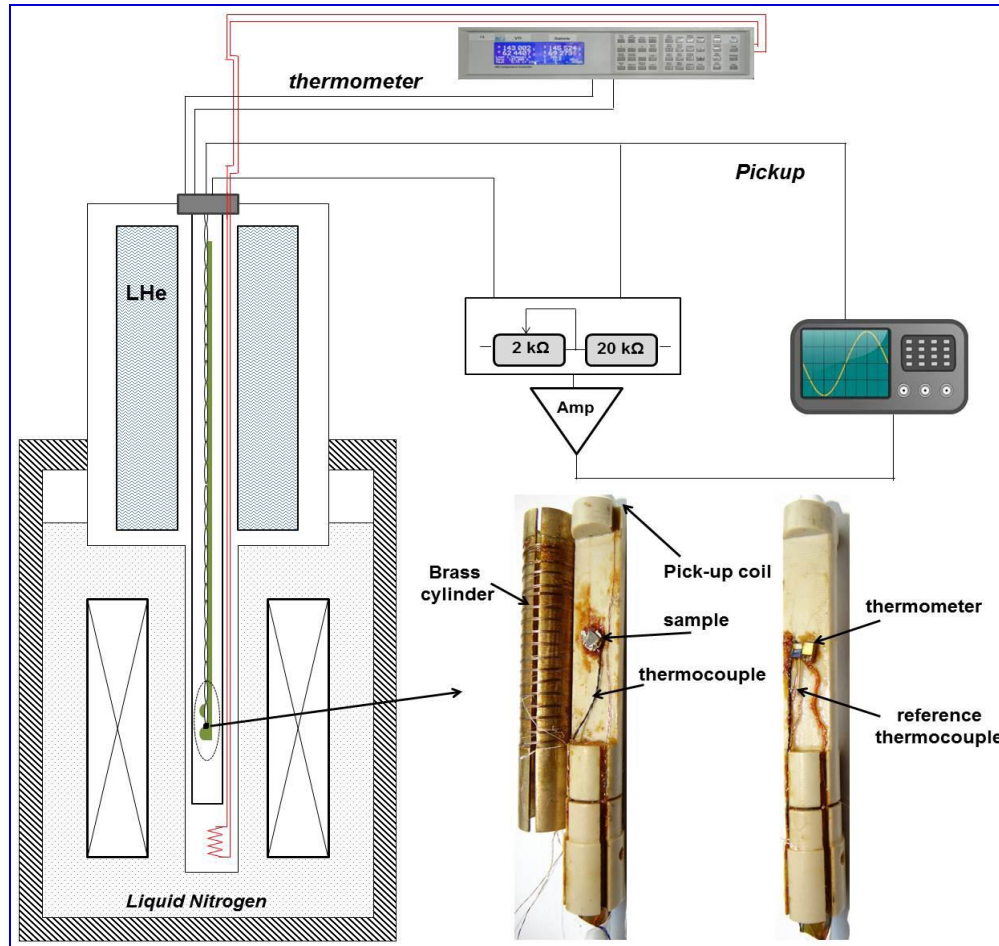
In this work, the small magnet used, designated “D” was used, which has a bore of 24 mm and operates with 1.5 MJ total energy, providing pulsed field up to 50 T and pulse length of 50 ms. Figure 3.13 (A) shows the time dependences of the magnetic fields obtained with different pulsed magnets operational at the HLD. The green curve corresponds to the used magnet and figure 3.13 (B) shows a photo of the used coil.

Figure 3.14 displays the set-up used in the measurements. A schematic drawing of the pulsed field experimental set-up containing the magnet, cryostat, sample holder, and electronic connections is shown and photos for both sides of the sample holder together with the local heater are provided.

As mentioned before, four equal samples (5mm×5mm×1mm) were prepared for these measurements, two of them were cut so that the shortest dimension was in [100]-direction and the other two with the shortest dimension in [001]-direction (Figure 3.15 A). In the beginning, the samples with the shortest dimension in [001]-direction were mounted in such a way that the field was parallel to the a- axis (easy direction).

A differential copper- constantan thermocouple was used to measure the temperature of the sample with wires diameter of 20 micrometers. The two wires (copper and constantan) were thoroughly twisted together to avoid any open loops (Figure 3.15 B), and then one leg of the thermocouple “sample junction” was fixed between the two samples and the other leg ”reference junction” was fixed on the other side of the holder to measure the temperature inside “reference temperature” and detect any influence of the field on the thermocouple voltage (Figure 3.14).

To make the junction between the two samples, two kinds of thermal-conductive epoxy (EPO-TEKH20E) were mixed in equal proportions. A very small amount of the mixture was placed at the surface of the first sample, the junction was put at the center of the sample and then the second sample was put on top resulting in a sandwich with the junction in the middle. The sandwiched sample was put on a heater for about one and half hour at 130 C° to stiffen out the epoxy. This was necessary to ensure good thermal contact and to decrease the heat loss between the measuring junction and the sample.



**Figure 3.14:** (a) Schematic of the experimental set-up for MCE measurements in pulsed magnetic fields (b) Pictures of both sides of the sample holder together with the brass cylinder [Zavareh, 2016].

After this, the two samples with the thermocouple junction between them were installed on the holder using GE varnish glue (Figure 3.15 C). The other junction was also installed with GE varnish at the same height on the other side of the holder, so that both junctions were subject to the same magnetic field (Figure 3.15 D). The sample holder with the wires was connected to a G10 rod with a length of 1.5 m. All electrical contacts were made of copper wires and all materials and wires used were chosen in order to minimize eddy currents.

After holding the system tightly, a local heater was placed around the sample to ensure uniform temperature distribution. The heater used was a brass cylinder with 0.5 mm thick wall and a diameter of about 12 mm with a longitudinal slit in it to prevent the production of eddy currents. Manganese wires of 50  $\mu$  diameter were bent and coiled around it as heating element and connected with the wires on the rod by solidification (Figure 3.15 E). Afterward,

the rod was covered by Teflon and enclosed in a thin-walled stainless-steel shield, and centered by spacers made from PEEK. During the mounting, four resistance measurements were regularly checked (heater, pick up coil, two lines of the thermometer, and thermocouple resistivity) to ensure that there was no open loop or shortage in the wires. Figure 3.15 (A) shows the four samples used in these measurements. Figure 3.15 (B) shows a schematic of the differential copper-constantan thermocouple and the front side of the sample holder with the samples mounted on it is shown in Figure 3.15 (C). The back side of the holder with the reference junction fixed on it is shown in figure 3.15 (D) and finally Figure 3.15 (E) shows the holder with the heater placed around the sample.

As the measurements had to be performed under adiabatic conditions, a pump was used to evacuate the sample space inside the shield. As in the case of pulsed magnetic fields the measurements are very fast, a limited vacuum is sufficient. The whole assembly was inserted into Helium-4 cryostat and the resistances were checked again.

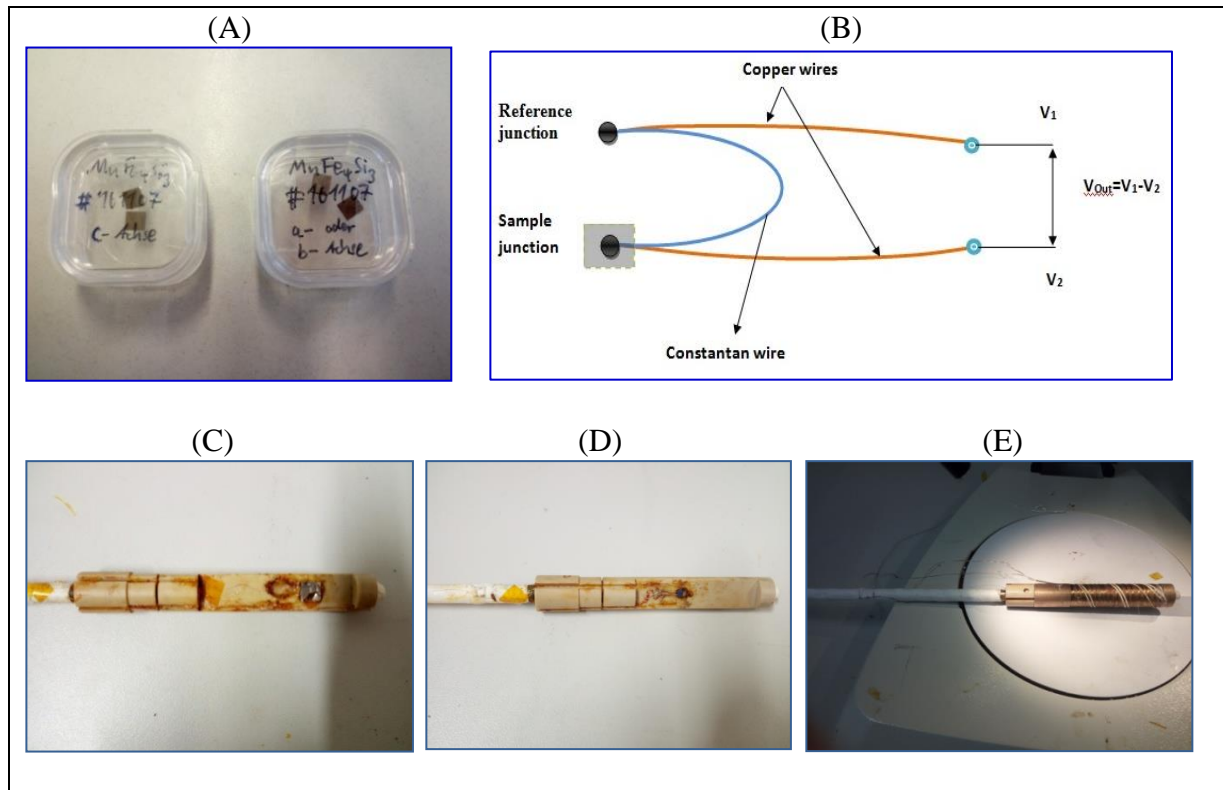


**Figure 3.15: The experimental setup: (A) the four samples used in these measurements (B) a schematic drawing of the thermocouple (C) the holder with the samples mounted (D) the back side of the holder with the reference junction installed (E) the holder with the heater placed around the sample.**

In the pulsed field measurements, it is very critical to measure the magnetic field precisely and in our work, this was done by measuring the induced voltage in a calibrated pick-up coil. In general, the pickup coil consists of a specific area (few mm<sup>2</sup>) with one or more turns of wires around it. In our case it was made of 15 turns of 60 μm isolated copper wire and situated at the end of the sample holder. The induced voltage was proportional to the time derivative of the enclosed magnetic flux,  $U_{\text{ind}}(t) \approx d\Phi/dt \approx dB(t)/dt$ , where  $B$  is the magnetic flux density. A digital oscilloscope (Yokogawa DL750 or DL850) with a sampling rate of up to 1 MHz was used for registering this voltage, then the digitized data were stored and integrated numerically to obtain the magnetic field as a function of time [**Zavareh, 2016**].

For a calibrated thermocouple, both  $V(T)$  and  $T(V)$  are defined in the form of polynomials. So the initial temperature  $T_i$  results in an initial voltage  $V_i$ . When the initial voltage is increased by the measured voltage change  $\Delta V$ , the final temperature  $T_f$  can be obtained from the inverse dependence  $T(V)$  and  $\Delta T = T_f - T_i$  can be calculated. For the conversion of the voltage difference in mV to the temperature change in K a Matlab program was used [**Zavareh, 2016**].

A large artificial voltage ( $dB/dt$ ) may arise from a small loop in the thermocouple wires. The provided the voltage change  $\Delta V$  which can be attributed to the magnetocaloric effect is significantly smaller than the artificial voltage. To prevent this disruption two measures were taken. An extra compensation circuit was used where the pick-up coil's compensation signal was passed through a voltage divider and the appropriate part of it was taken and subtracted from the thermocouple signal. Secondly we made use of the fact that the MCE does not depend on the field direction. Therefore, averaging between positive and negative pulses allows extracting the required temperature-dependent part of the voltage signal. By using these two methods, it was possible to remove the effect of  $dB/dt$  from the measured results.

After applying this procedure, the signals from the thermocouple were amplified and conditioned by a low-noise voltage amplifier (FEMTO-DLPVA). The time-dependent thermocouple signal  $\Delta V(t)$ , was recorded by a digitizer and later converted to  $\Delta T_{\text{ad}}(t)$  with the already mentioned Matlab program [**Zavareh, 2016**].

Initially, 2 T pulses (1 KV) were applied at different initial temperatures and the value of  $\Delta T_{ad}$  was calculated for each temperature. Then the same procedure was performed with 20 T pulses (10 KV) at slightly different temperatures, and finally one 50 T pulse (24 KV) was applied at 320 K to obtain the value of  $\Delta T_{ad}$  at this high magnetic field. Table 3.1 shows the initial temperatures at which the pulses were applied.

**Table 3.1: The initial temperatures at which the pulses were applied.**

2T Pulses	20T Pulses	50T Pulses
340	330	320
330	320	
320	315	
310	310	
305	305	
300	300	
295	280	
290	260	
285		
275		
265		
255		

The second sample was mounted in place (with the field parallel to c-axis) after dismounting the first. A test pulse of 10 T, which was applied at 340 K, did not result in data of sufficient quality as the heat transfer between the sample and the thermocouple was too slow. This was evident from an offset between the measured temperature and the real temperature of the sample. Due to the limited magnetic time available, the measurements on this sample were stopped. And the sample was pulled out and cut for magnetization measurements.

## Data Analysis and Discussion

### 4.1 Le Bail Refinements of the Powder Diffraction Data

LeBail refinements [LeBail et al., 1988] were performed with the program Jana 2006 [Petricek et al., 2006]. According to the previous literature, the compound  $\text{MnFe}_4\text{Si}_3$  crystallizes in a hexagonal structure in the space group  $P6_3/mcm$  with lattice parameters  $a = b = 6.8043(4) \text{ \AA}$ , and  $c = 4.7254(2) \text{ \AA}$  [Gourdon et al., 2014] and these parameters were used for the starting model. A manual background was defined and for profile fitting the pseudo-Voigt-function with parameters GW and LX was used. In addition, the zero shift was refined.

Figure 4.1 displays the final Le Bail refinement. The difference between the observed and the calculated diffraction diagram is small (final  $wR_p = 0.82\%$ ) and there are no indications of impurity phases.

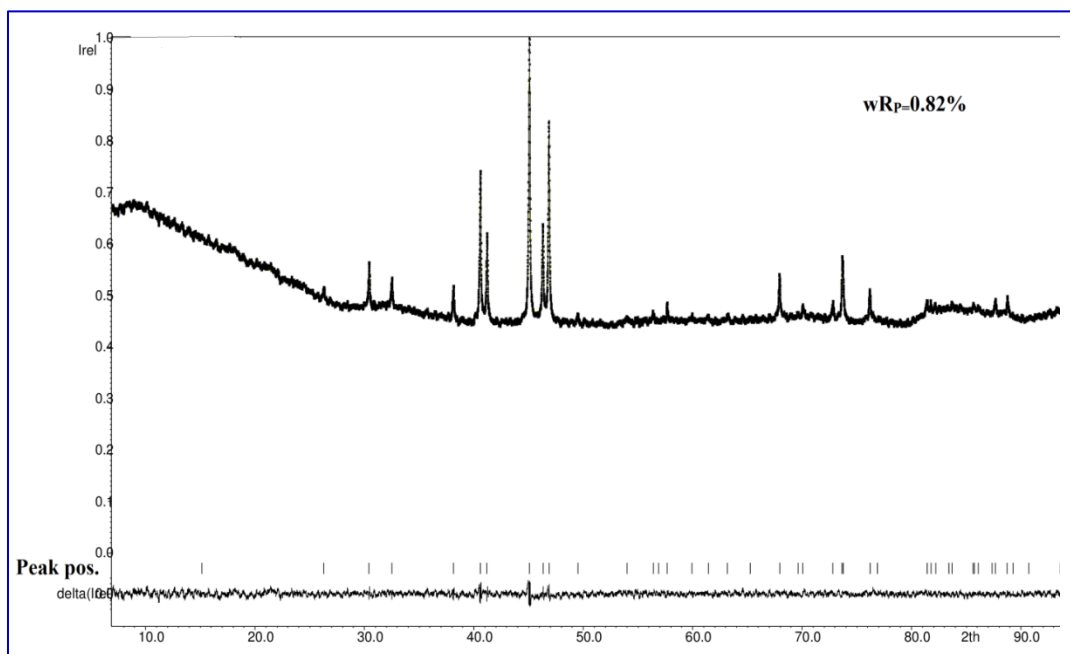


Figure 4.1: Observed intensities and the difference profile of  $\text{MnFe}_4\text{Si}_3$  measured at room temperature from the LeBail refinement.

## 4.2 Macroscopic Properties

### 4.2.1 Magnetization measurements

#### 4.2.1.1 Magnetization measurements in DC field

The magnetic properties of the sample were investigated by measuring the magnetic moment vs. the magnetic field. The magnetization is calculated from the measured magnetic moment per unit mass ( $\text{Am}^2/\text{Kg}$ ). The errors in the measurements of sample masses yield an error in the magnetization of about  $\pm 1.0 \times 10^{-5} \text{Am}^2/\text{Kg}$ .

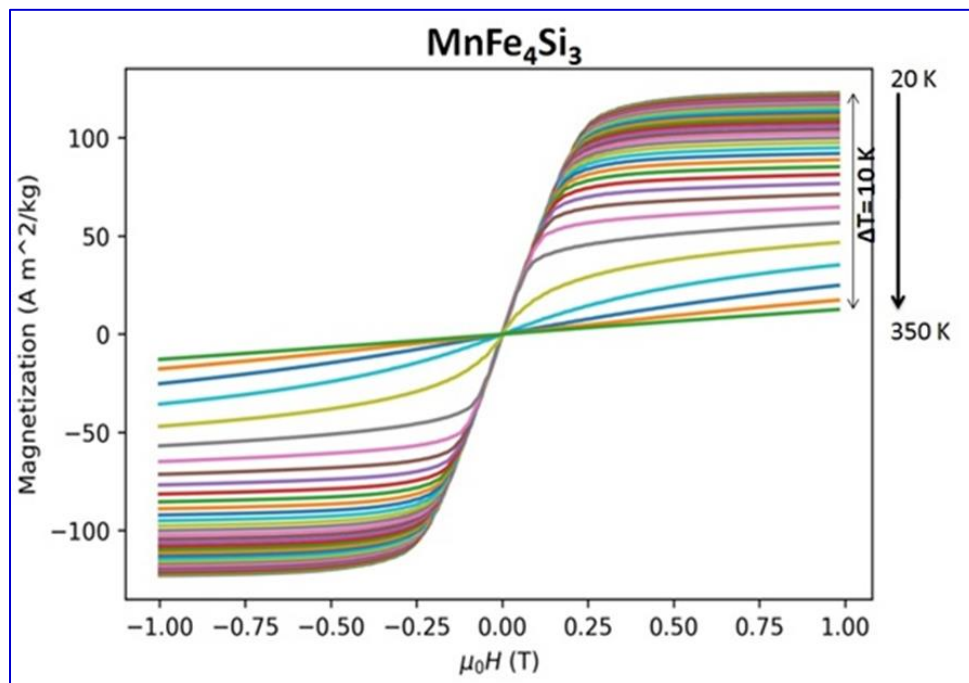


Figure 4.2: Hysteresis loops of  $\text{MnFe}_4\text{Si}_3$  measured at temperatures from 20-350 K ( $H \parallel [100]$ ).

Figure 4.2 shows the  $\text{MnFe}_4\text{Si}_3$  magnetization as a function of the applied magnetic field parallel to the crystallographic a-axis ( $H \parallel [100]$ ) for values up to 1T and the temperature range is shown. In the ordered phase one can distinguish steep linear field dependence at small fields and a second linear region with a small slope at larger fields. I have analyzed each curve by fitting with a linear function in each region (Figure 4.3 as a case).

Using the data I have calculated the magnetic susceptibility  $dM/dH$  in the region around zero field (Figure 4.4 top, where  $dM/dH$  changes drastically at the transition temperature) and the

spontaneous magnetization by extrapolating the saturation data to zero field (Figure 4.4 bottom). Figure 4.4 middle shows the  $dM/dH$  slopes for the saturated data from a fit with a straight line. For low temperatures or ordered states the slope is constant, while close to the transition temperature the model breaks down, as we do not preserve saturation and the magnetization changes linearly. This is also the reason for the broadening of the transition as can be inferred from the spontaneous magnetization.

For temperatures below 300 K, the slope around zero field is constant. The magnetization approaches  $120.30(5) \text{ Am}^2/\text{Kg}$  at a field of 0.4 T and a temperature of 20 K. For higher fields, there is a small linear increase and up to 1 T there is no clear saturation. Upon increasing the temperature, the sharp transition is gradually broadened and the value of saturation magnetization decreases (Figure 4.4 bottom).

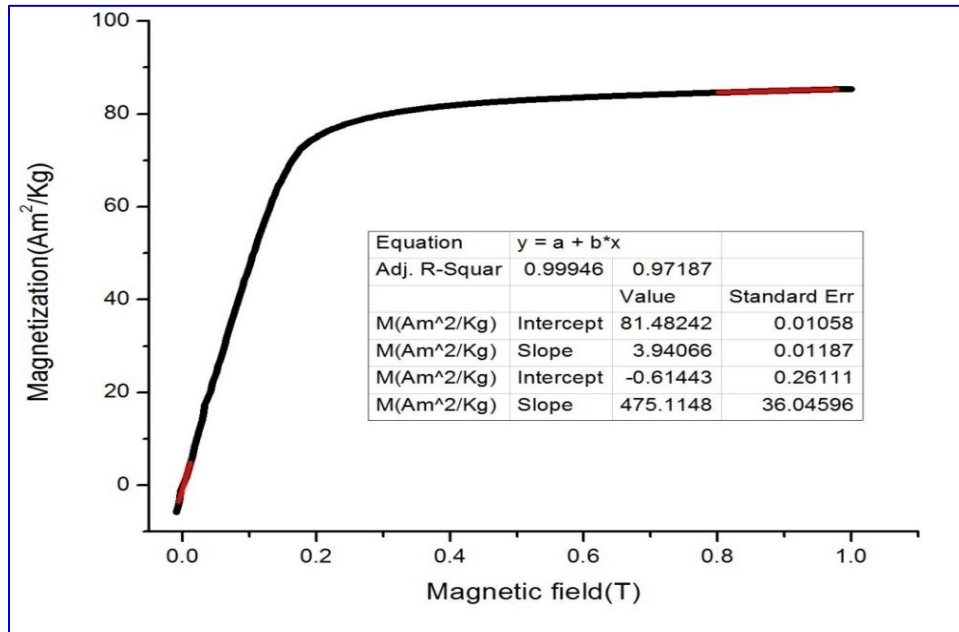
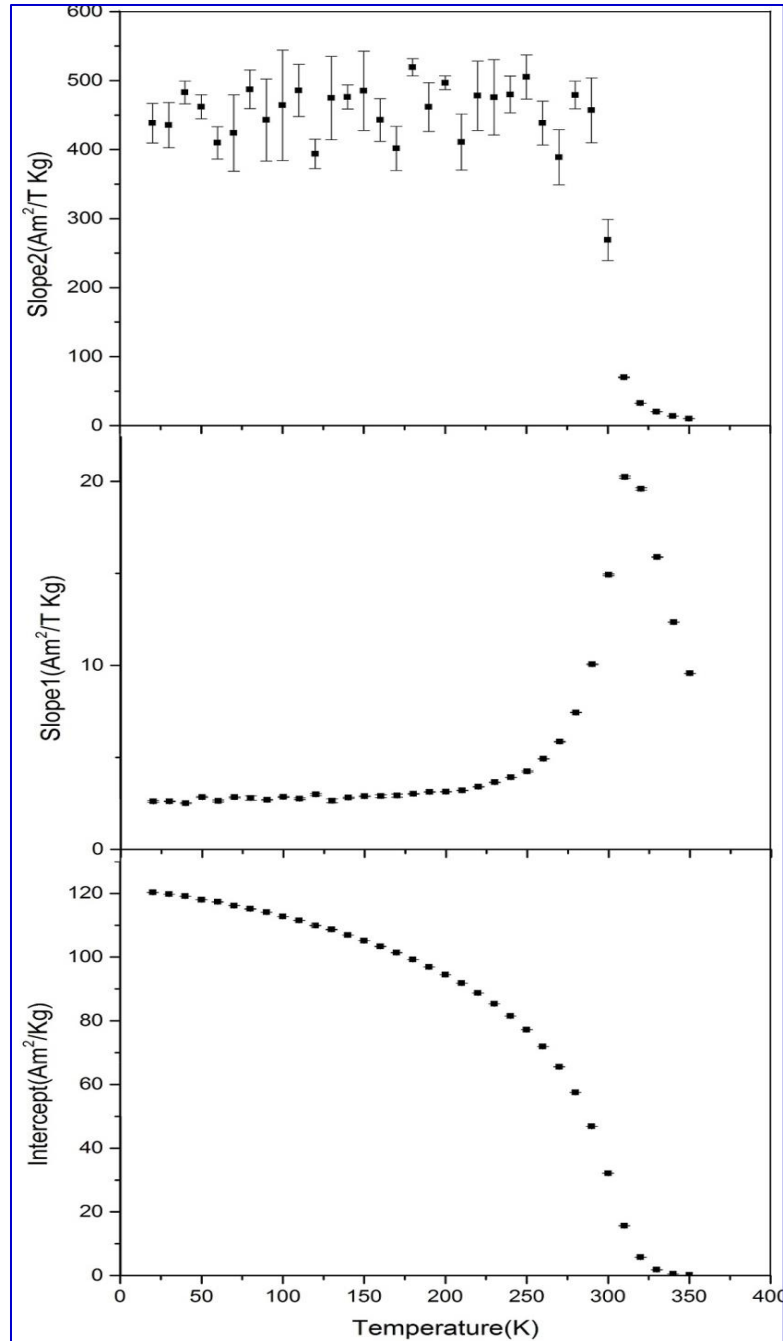


Figure 4.3: Hysteresis loop measured at 240 K with the linear function fitting ( $H \parallel [100]$ )

Close to the transition temperature and above, the aforementioned model does not hold any more. The slope at small fields changes drastically and the saturation is not reached at 1 T. At 330 K and above, the magnetic moment increases linearly with the field in the measured range and the sample shows a paramagnetic behavior. Comparing with [Hering et al., 2015], a good agreement can be seen with a slightly smaller values of the maximum magnetization and the field of saturation in our results.



**Figure 4.4:** Bottom: magnetization in the saturation region; Middle: slopes in the saturation region; Top: slopes in the region near zero field,  $H \parallel [100]$ . Error bars are shown if they exceed the symbols size.

Figure 4.5 shows the hysteresis loops of  $MnFe_4Si_3$  with the field parallel to the crystallographic c-axis ( $H \parallel [001]$ ). Comparing with the hysteresis loops with the field parallel to a-axis, we can see a clear anisotropy of the magnetic response. Again, in the ordered phase one can distinguish the linear field dependence at small applied fields (albeit less steep than in  $[100]$  case) and a second linear region with a small slope at large fields.

However the model of two linear regions breaks down earlier than the [100] case. I also have analyzed each curve similar to the [100] direction (Figure 4.6 as a case).

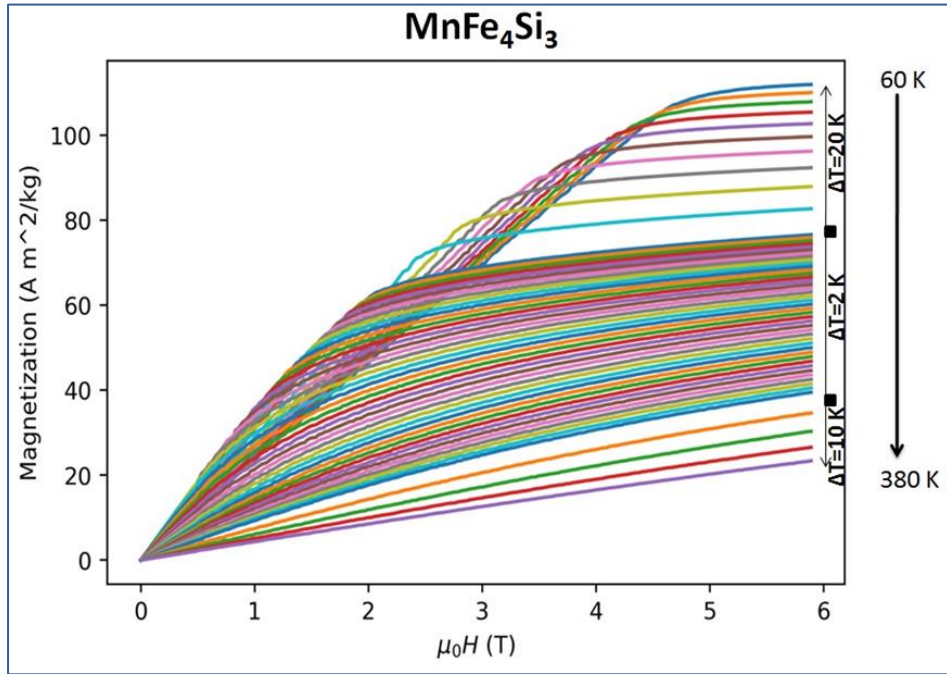


Figure 4.5: Hysteresis measured at temperatures from 60-380 K ( $H \parallel [001]$ ).

I calculated the magnetic susceptibility  $dM/dH$  in the region around zero field (Figure 4.7 top), where a very sharp peak can be seen at the transition temperature and the spontaneous magnetization by extrapolating the high field data to zero field (Figure 4.7 bottom)

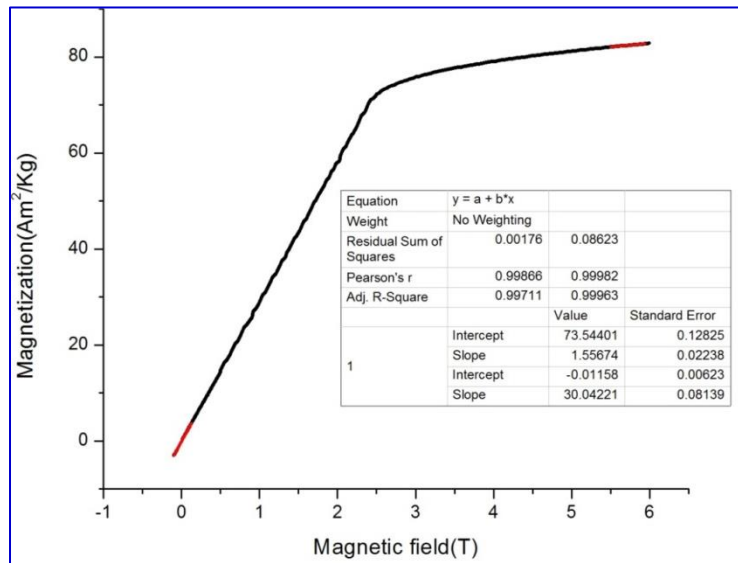
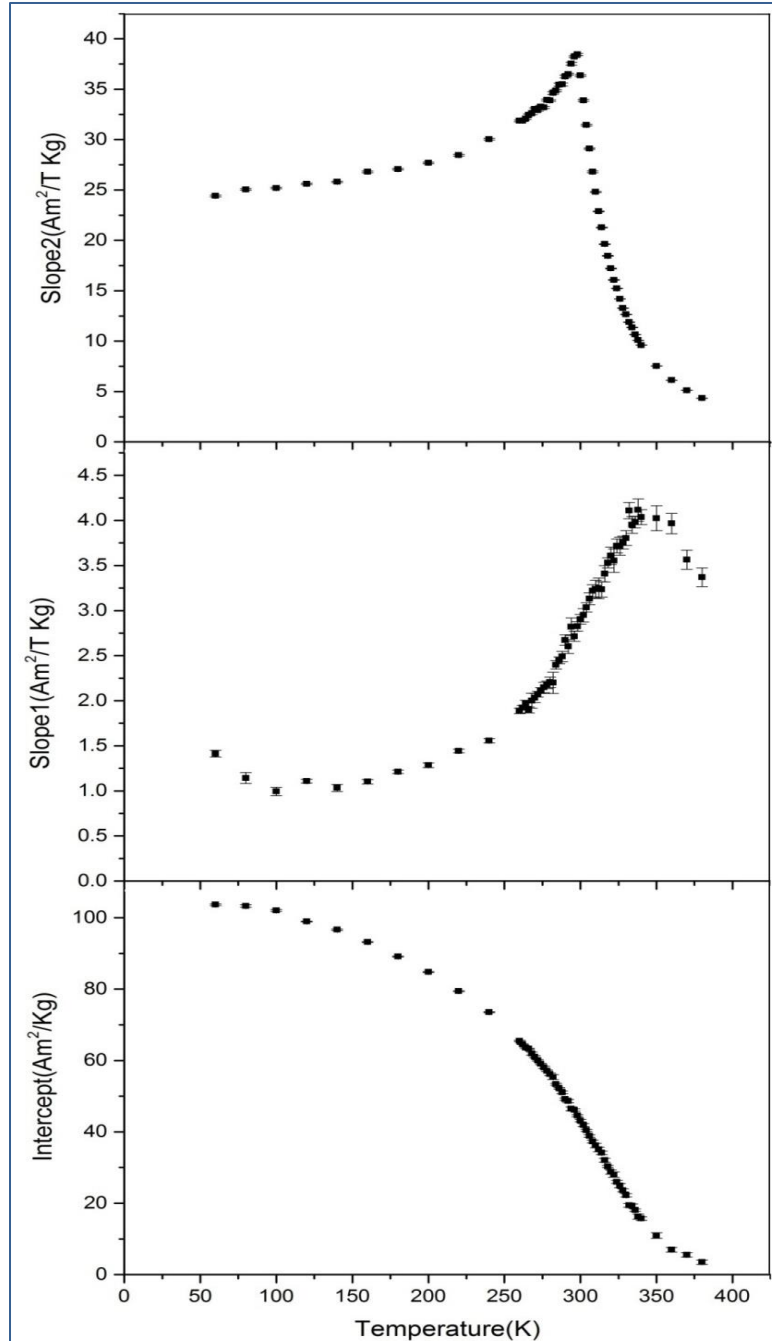


Figure 4.6: Hysteresis loop measured at 240 K with the linear function fitting ( $H \parallel [001]$ ).



**Figure 4.7: Bottom: magnetization in the saturation region; Middle: slopes in the saturation region; Top: slopes near zero field region.  $H \parallel [001]$ . Error bars are shown if they exceed the symbols size.**

In these hysteresis loops, It can be seen that the of the magnetization field dependence increases slower and reaches smaller maxima compared to the [100] direction. For example the magnetization reaches about 103.64 (22) Am<sup>2</sup>/Kg at a field of 5 T at 60 K, and then at a higher fields, there is a small linear increase and up to 6 T there is no clear saturation. This

agrees with [Hering et al., 2015] as no saturation was obvious in a field up to 4 T. These observations confirm that for the compound  $\text{MnFe}_4\text{Si}_3$ , the magnetization easy axis is in the a,b-plane and the c-direction is the hard magnetization axis.

After 300 K, the magnetization dependence on the field increases, the slopes of the saturation region increase, and the saturation starts to weaken (Figure 4.7, middle). At 380 K, the magnetic moment loses saturation and increases linearly with the field.

For the calculation of the MCE from the hysteresis measurements, the temperature dependent magnetic response for different field values applied parallel to [100] is shown in Figure 4.8. The response for the field parallel to [001] is shown in Figure 4.9 (see also, Figure A4). We can see the difference between the magnetization values for the two directions at the same field value.

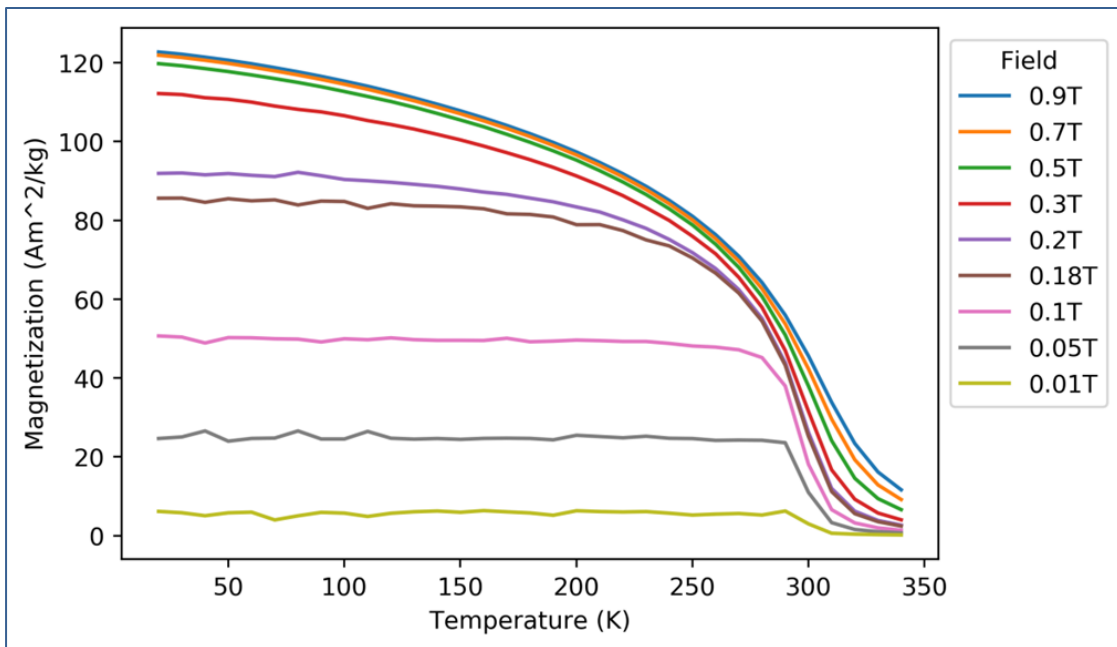


Figure 4.8: Temperature-dependent magnetization of  $\text{MnFe}_4\text{Si}_3$  from hysteresis measurements ( $H \parallel [100]$ )

The anisotropy is also visible in the temperature dependence. In the [100] direction, the magnetization quickly reaches a constant value for small applied fields ( $\mu_0 H < 0.2$  T). For larger fields the typical temperature dependence of a ferromagnets develops, approaching saturation only at low temperatures. For the [001] direction the shape is completely different.

$M(T)$  features a maximum, which shifts with increasing field to lower temperature. For the higher fields it becomes shallower and might finally disappear for  $\mu_0 H > 5T$  (as measurement below 60 K where not performed, it could also move to a lower temperature range). Even at the lowest temperature and highest field, the magnetization for [001] is still lower than the [100] direction. Please refer to the measurements in pulsed fields (4.2.1.2).

For higher temperatures, the curves show the largest slope for an applied field parallel to [100] and hence a large entropy change is expected (based on Maxwell's relation

$$\Delta S(T) = \int_H^0 \left( \frac{\partial M}{\partial T} \right) dH.$$

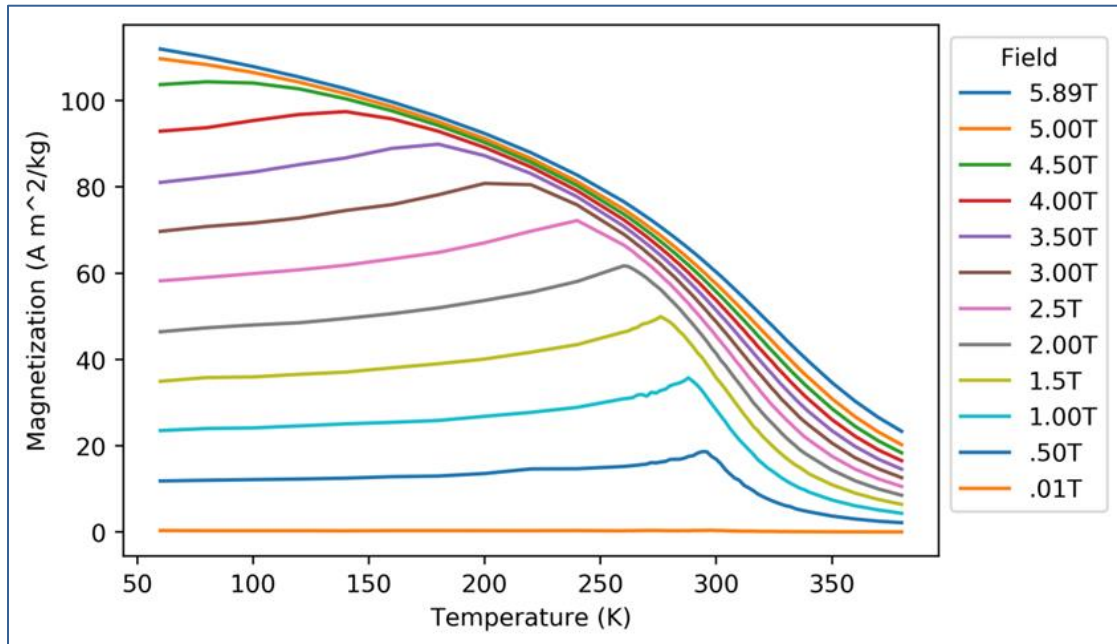


**Figure 4.9:** Temperature-dependent magnetization of  $MnFe_4Si_3$  from hysteresis measurements ( $H \parallel [001]$ )

With an applied field along the a-axis, the magnetic entropy change has a maximum of about 1.3 J/kgK for a field change of 1 T, and with the field along the c-axis, the magnetic entropy change has a maximum of about 3.5 J/kgK for a field change of 6 T (or 0.583 J/kgK per 1 T) which is smaller than the a-axis value. This is consistent with the values reported by [Hering et al., 2015] which are 2.9 J/kgK and 1.3 J/kgK for 2 T along the a-axis and c-axis respectively. These observations demonstrate that the MCE in this compound is clearly dominated by the magnetic moments aligned in the a,b-plane.

Figures 4.10 and 4.11 display the isothermal entropy change  $\Delta S$ , which serves as a measure of the MCE, calculated from Maxwell's relation based on the measured magnetic hysteresis loops with fields along the [100] and [001] directions respectively. From the two curves the magnetocaloric effect also shows a significant anisotropy with a maximum value approximately at 300 K (i.e. largest at the temperature of the magnetic phase transition).

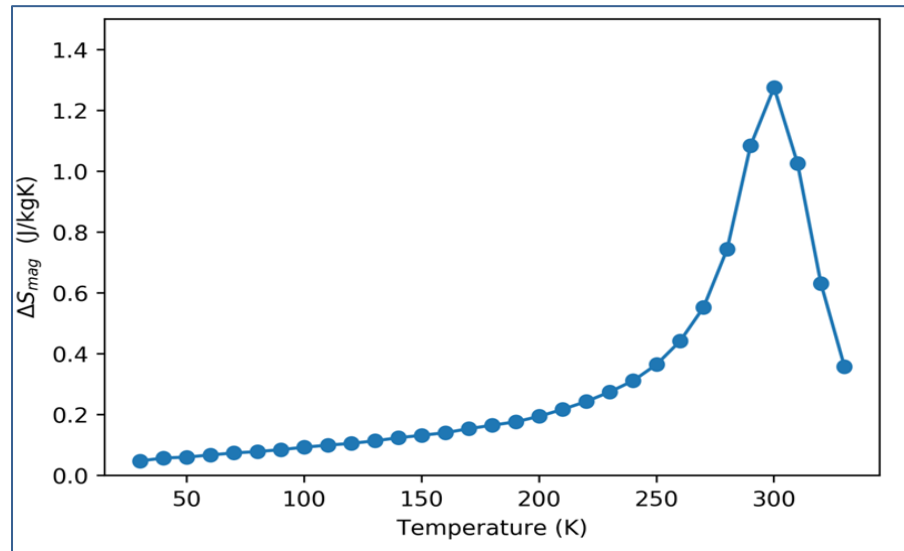


**Figure 4.10:** MCE of  $\text{MnFe}_4\text{Si}_3$  calculated from the temperature-dependent magnetization at a field of 1T ( $\mathbf{H} \parallel [100]$ ).

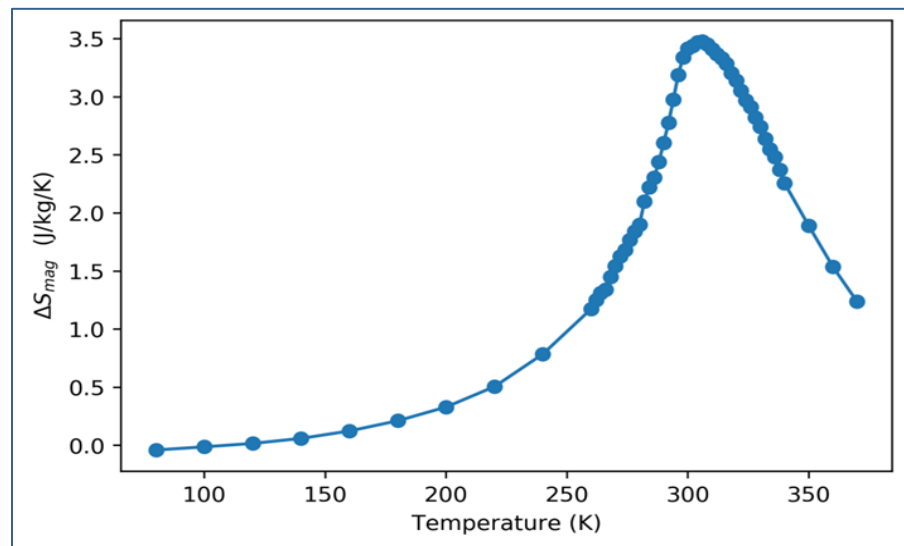


**Figure 4.11:** MCE of  $\text{MnFe}_4\text{Si}_3$  calculated from the temperature-dependent magnetization at a field of 6T ( $\mathbf{H} \parallel [001]$ ).

#### 4.2.1.2 Magnetization measurements in a pulsed field

Figure 4.12 shows the field dependent magnetization  $M(H)$  obtained from the pulsed magnetic field experiment together with isothermal magnetization data measured in a field up to 8 T at 5 K in the [100] direction. The pulsed field magnetization measurement data was normalized to the DC field data at 8 T.

It can be seen that there is an excellent agreement between the two curves. A steep rise in magnetization occurs in both curves and reaches about  $126.41(30) \text{ Am}^2/\text{Kg}$  for the DC data and a slightly lower value in pulsed data ( $119.98(23) \text{ Am}^2/\text{Kg}$  at a field of 8 T). The pulsed measurement reaches saturation at 0.25 T which is a slightly smaller field than the DC measurement (0.3 T). At higher fields, there is a small linear increase which is larger in the pulsed field curve (for the pulsed field the approach to saturation is smoother, and holds for both measurements a long [100] [001] directions). However we can say the two curves are comparable and the slope variation could be a result of the different instrumentations used.

A first order transition is evident from the data measured along [100] direction and that clearly identifies [100] as the easy direction for magnetization.

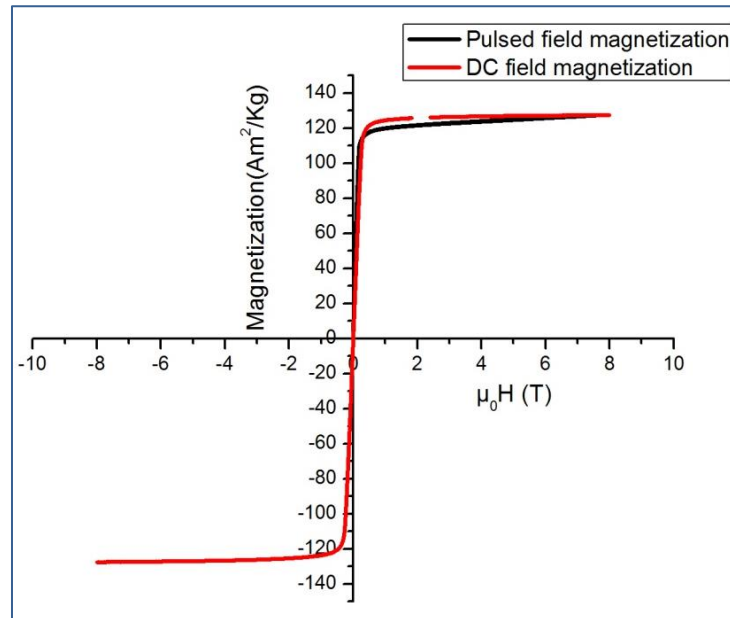
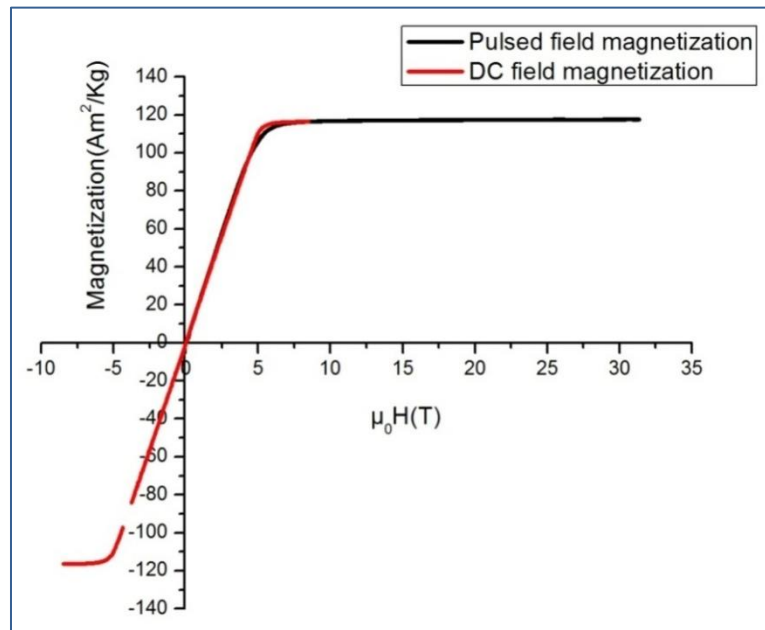


Figure 4.12:  $M(H)$  curves in pulsed magnetic field and DC field at 5 K in [100] direction.

Figure 4.13 shows the field- dependent magnetization  $M(H)$  measured in pulsed magnetic field up to 30 T together with the isothermal magnetization measured in DC field up to 8.5 T both at 5 K in [001] direction. The pulsed field magnetization measurement data was normalized to the DC field data at 8.5 T.

Again an excellent match between the two curves can be seen. The magnetization increases slower compared to the [100] direction. It reaches about  $114.16(7) \text{ Am}^2/\text{kg}$  at 5.5 T for the DC field and  $116.59(1) \text{ Am}^2/\text{kg}$  at 7 T for the pulsed field, and at higher fields, there is a small linear increase. Comparing the pulsed field measurements in [100] and [001] directions, the magnetic anisotropy of the sample is obvious.



**Figure 4.13:  $M(H)$  curves in pulsed magnetic field and DC field at 5 K with the field applied in [001] direction.**

#### **4.2.2 Direct measurements of the magnetocaloric effect in pulsed magnetic fields**

The main advantage of these measurements is that they are performed under adiabatic conditions ensured by the sufficiently fast magnetic-field change (short pulse duration). In addition, the accessible magnetic field range extends beyond 70 T.

Figure 4.14 shows the adiabatic temperature change for the easy direction of a  $\text{MnFe}_4\text{Si}_3$  single crystal sample as obtained from the direct measurements in pulsed magnetic field of 2 T (black symbols) and 20 T (red symbols). It is obvious that  $\Delta T_{\text{ad}}$  increases with increasing the applied magnetic field.

A maximum  $\Delta T_{\text{ad}}$  occurs at  $T_C$  (300K) for a field change of 2 T. With increasing the magnetic field up to 20 T, the observed peak broadens, extending towards higher temperatures. This can be explained as follows: at temperatures below  $T_C = 300$  K, the sample is in a ferromagnetic state and applying a magnetic field only marginally changes the entropy of the system and consequently the change in  $\Delta T_{\text{ad}}$  is comparatively small. Since at  $T_C$  the magnetization changes quickly because of the field-induced first-order transition, an MCE maximum is expected around  $T_C$  (according to Maxwell's relation:  $\Delta S(T) = \int_H^0 \left(\frac{\partial M}{\partial T}\right) dH$ ). Above  $T_C$ , an applied magnetic field can induce the transition-provided the temperature is not too high above  $T_C$  resulting in an entropy jump.

Depending on the field strength, the induced transition can be complete or incomplete. In the case of an incomplete transition, the transformation is partial and  $\Delta T_{\text{ad}}$  is correspondingly lower. This is visible as a decrease in  $\Delta T_{\text{ad}}$  above  $T_C$  (2 T data in Fig. 4.14). According to the magnetization data discussed before, a maximum field of 20 T is sufficient to complete the transition at any considered temperature. Thus, at 20 T the MCE maximum extends towards higher temperatures and  $\Delta T_{\text{ad}}$  displays a broad maximum. The  $\Delta T_{\text{ad}}$  reduction above 315 K is because the height of the magnetization jump, and thus the associated transition entropy decreases considerably. This broad maximum is also reported in [Fujieda et al., 2002] for the  $\text{La}(\text{Fe,Si})_{13}$  system and for the  $\text{La}(\text{Fe,Si,Co})_{13}$  system [Zavareh, 2016].

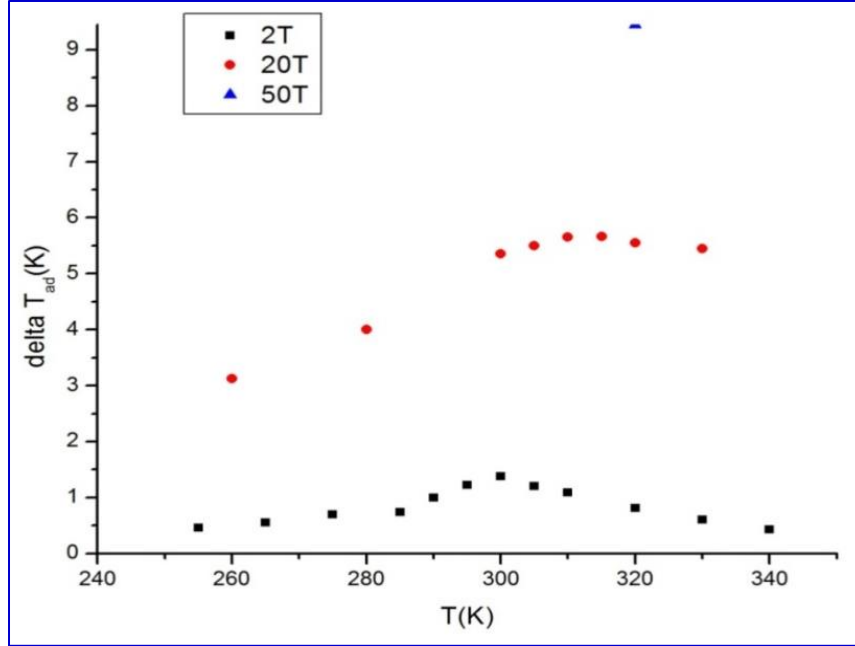


**Figure 4.14: Comparison of  $\Delta T_{ad}$  for  $MnFe_4Si_3$  measured in pulsed magnetic fields of 2 T (black symbols), 20 T (red symbols) and 50 T (blue symbol).**

The maximum values of  $\Delta T_{ad}$  were 1.38 and 5.66 K for field changes of 2 T and 20 T, respectively. The adiabatic temperature change increases only by a factor of 4 when the field increases by a factor 10. The MCE for the  $MnFe_4Si_3$  single crystal measured under pulsed field up to 50 T for the temperature 320 K gave a  $\Delta T_{ad}$  value of 9.45 K (blue symbol).

Gd is considered as the benchmark for the magnetocaloric materials comparisons. This is because it has a Curie temperature close to room temperature ranging 289-295 K according to literature [Dan'kov et al., 1998]. It has small to no anisotropy; a negligible magnetic-hysteresis losses; and more importantly a large MCE [Hansen, 2010]. For polycrystalline samples of Gd direct measurements in pulsed magnetic fields of 6.5 and 70 T under adiabatic conditions were performed. Around the Curie temperature, the maxima of  $\Delta T_{ad}$  were 13 and 60 K, respectively [Zavareh, 2016]. By comparing these values with our results values of  $\Delta T_{ad}$  for  $MnFe_4Si_3$ , Gd has a much larger MCE, which is expected because the magnetic moment of Gd is much larger.

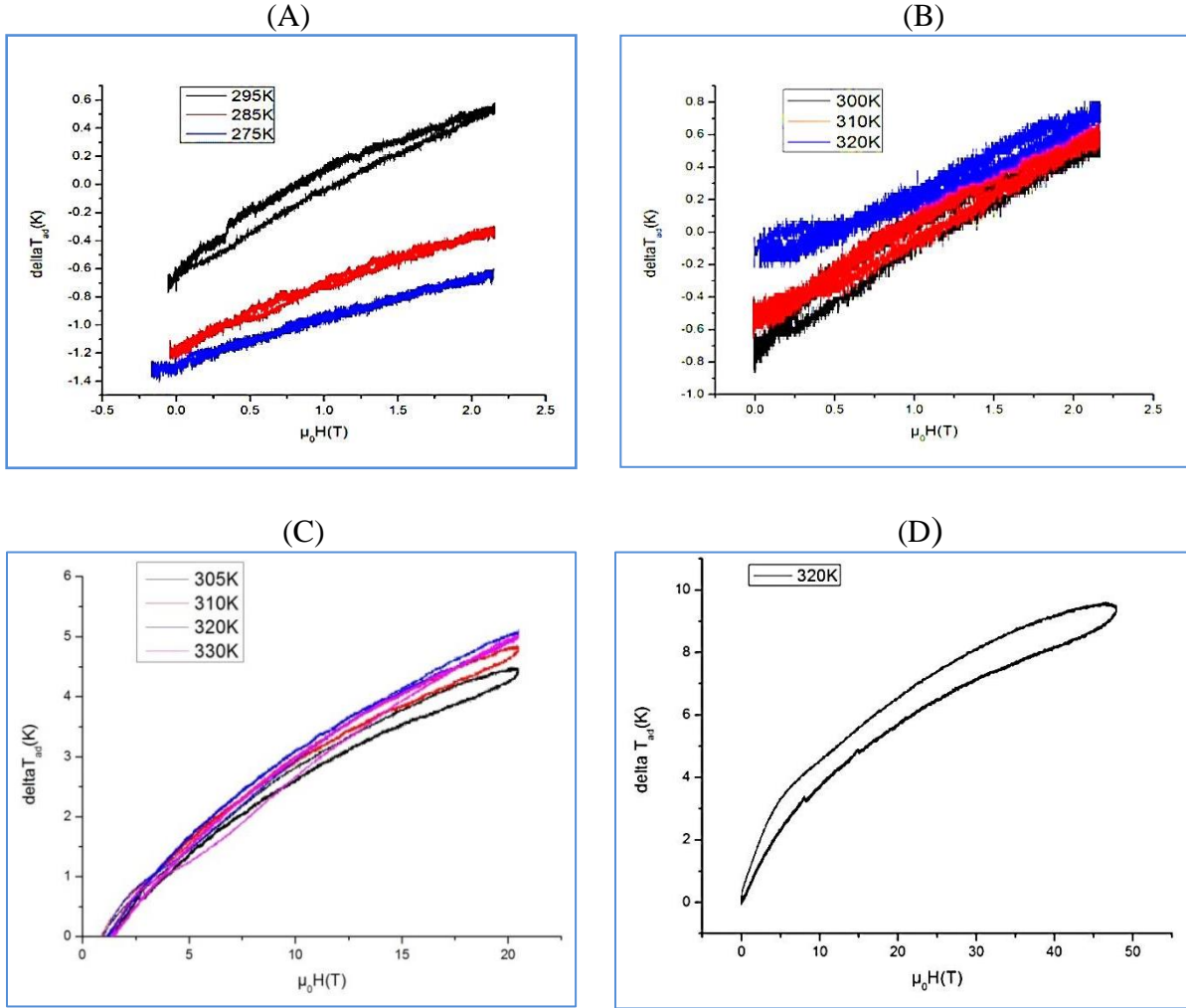


**Figure 4.15: field dependence of  $\Delta T_{ad}$  for different initial temperatures and a pulsed field change of (A, B) 2 T (C) 20 T (D) 50 T.**

However, the interesting comparison would be at lower fields, e.g. 1 or 2 T as it is the used fields for applications, and according to [Gschneidner et al., 2012; Hansen, 2010]  $\Delta T_{ad}$  for Gd in the field of 2 T is approximately 5.5 K (deduced from magnetization measurements) and that is larger for Gd by a factor of three compared to  $\text{MnFe}_4\text{Si}_3$ . However, if we count other factors important for the applicability of the material including cost, and mechanical stability,  $\text{MnFe}_4\text{Si}_3$  might be a better candidate.

Figure 4.15 shows the field dependence of the adiabatic temperature change for different initial temperatures around  $T_C$  for a field change of (A and B) 2 T (C) 20 T (D) 50 T. From the figures it is clear that the magnetization and demagnetization curves nearly coincide, (the

short pulse time is not detrimental for the response time of the thermocouple) which underscores these measurements is reversible (adiabatic condition).

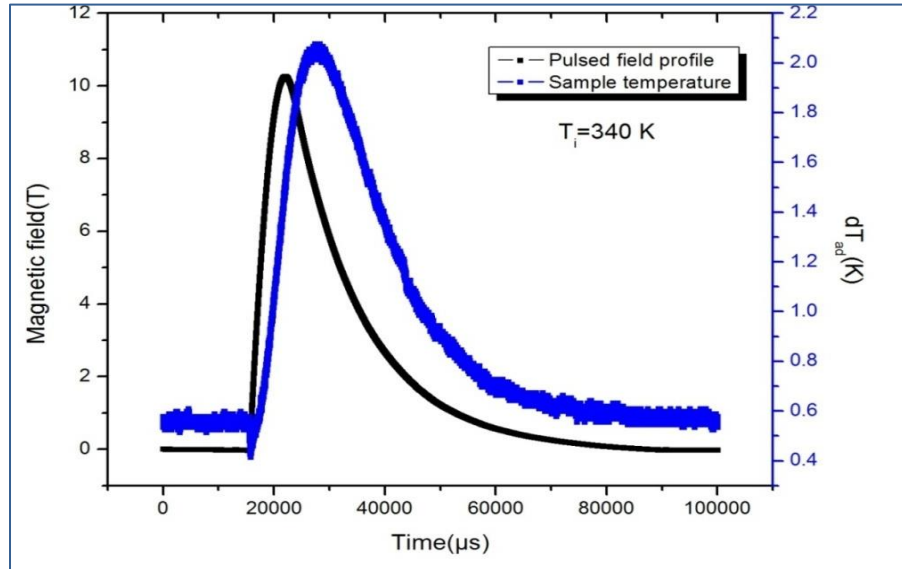


**Figure 4.16: Time dependences of the adiabatic temperature change in pulsed magnetic field of 10 T at 340 K.**

Figure 4.16 displays the time dependence of  $\Delta T_{ad}(t)$  for the  $MnFe_4Si_3$  sample at a 340 K under a pulsed field of 10 T in the [001] direction (blue curve) together with the corresponding pulse profile (black curve). It can be seen that the heat transfer between the sample and the thermocouple was too slow (imperfect sandwich), and the measured temperature measurement was slightly delayed which means it does not correspond to the real temperature of the sample and the measurement is not fully reversible. A bump appearing at the beginning of the  $\Delta T_{ad}(t)$  curve, is a result of a small open loop in the thermocouple wires that acted as a magnetization pickup coil.

Figure 4.17 shows how a reversal of the field polarity affects the sign and magnitude of the bump, confirming it is not related to the MCE response. To minimize this effect we took the average of two measurements taken for the positive and the negative of the field pulse.

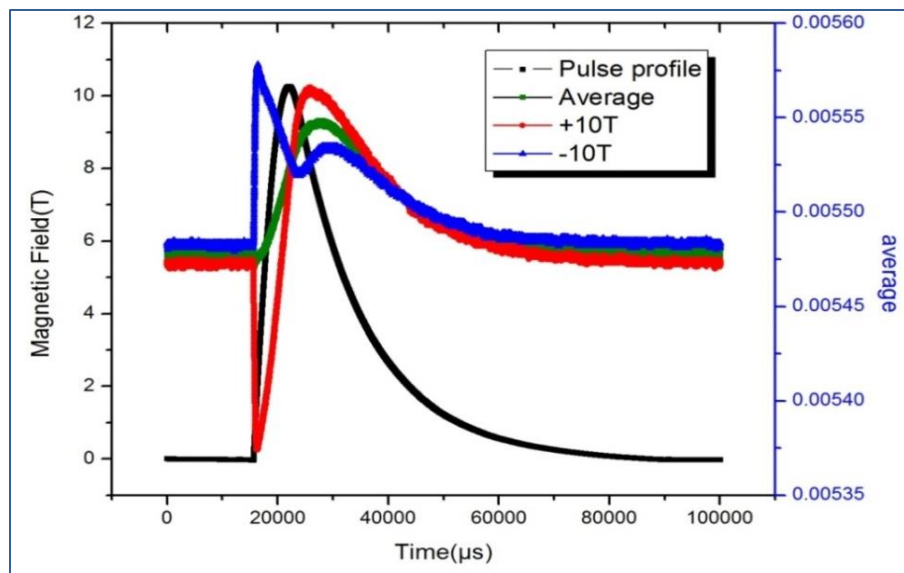


**Figure 4.17: The time dependence of  $\Delta T_{ad}$  with pulsed fields of +10 T and -10 T at 340 K and the average of the two.**

## Conclusions and Future Work

---

### 5.1 Conclusions

In this thesis, a single crystalline sample of composition  $\text{Mn}_{5-x}\text{Fe}_x\text{Si}_3$   $x=4$  was prepared. The phase purity was confirmed by a LeBail refinement of the x-ray powder diffraction diagram of the grinded sample. Laue diffraction was used to define the orientation of the crystal. The crystal was then cut in an oriented way for further characterization measurements.

The magnetic and magnetocaloric properties of single crystalline  $\text{MnFe}_4\text{Si}_3$  were studied. The magnetization and MCE were measured in both constant and pulsed fields. As a strong magnetic anisotropy was observed, the measurements were done with an applied field along [100] direction and along [001] direction.

Magnetization measurements in DC fields (hysteresis loops  $M(H)$ ) confirm that the easy axis of magnetization lies in the a,b-plane. The field dependence of the magnetic moments shows that the compound undergoes transition to a ferromagnetic ordered phase at approximately 300 K.

The isothermal entropy change  $\Delta S$ , which serves as a measure for the MCE, was calculated from Maxwell's relation based on the measured magnetic hysteresis loops. It was found that the MCE is larger with an applied field along the a-axis. In this case the magnetic entropy change has a maximum of about 1.3 J/kgK for a field change of 1 T. If the field is applied along the c-axis a maximum of about 3.5 J/kgK for a field change of 6 T is observed.

Magnetization measurements in pulsed field up to 8 T in [100] direction and up to 30 T in [001] direction were also performed. The data was normalized to the DC field data at 8 T for [100] direction and 8.5 T for [001] direction. In general, a very good match between the data

using static and pulsed magnetic fields was observed and only small apparatus dependent discrepancies were found.

We have investigated the magnetocaloric effect (MCE) of single crystalline  $\text{MnFe}_4\text{Si}_3$  sample by direct magnetocaloric measurements in pulsed magnetic fields, providing the temperature and field dependence of the adiabatic temperature change.  $\text{MnFe}_4\text{Si}_3$  displays a first-order phase transition with a Curie temperature of about 300 K. The MCE exhibits magnetic-field dependence, the maxima of  $\Delta T_{\text{ad}}$  are found to be 1.38 and 5.66 K for a field change of 2 and 20 T, respectively. Also for the first time, we measured the MCE in a single crystalline  $\text{MnFe}_4\text{Si}_3$  in pulsed magnetic fields up to 50 T and a large adiabatic temperature change of 9.45 K was observed.

## 5.2 Future Work

For the future work, there will be a focus on the synthesis of materials in the ternary systems Mn-Fe-Si, Mn-Co-Sb and/or Ni-Mn-Si and aim at the optimization of the properties through doping with different elements. The materials will be investigated with elastic and inelastic neutron measurements at neutron instruments, macroscopic magnetization and specific heat measurements, synchrotron measurements (in particular x-ray magnetic circular dichroism to probe the magnetic ordering element specific) and the direct determination of the temperature change in the material by using pulsed magnetic fields at the high field facility of the Helmholtz Society in Dresden Rossendorf. In addition, an experimental setup for the in-house measurement of the adiabatic temperature change will be developed. Finally suitable candidate materials will be identified to gain a deeper understanding of the coupling between the spin and lattice degree of freedom in these materials.

## Bibliography

[Beys and Gier, 2014] M. Beys and H. Gier, private communication, Forschungszentrum Jülich GmbH (2014).

[Binczycka et al., 1973] H. Binczycka, Z. Dimitrijevic, B. Gajidand, A. Szytuu, *Atomic and Magnetic Structure of  $Mn_{5-x}Fe_xSi_3$* , *physicstatus solidi*, 19, K13 (1973).

[Birkholz, 2006] M. Birkholz, *Thin Film Analysis by X-Ray Scattering*, WILEY-VCH Verlag GmbH & Co. KGaA, Weinheim (2006).

[Brown, 1976] G.V. Brown, *Magnetic heat pumping near room temperature*, *Journal of Applied Physics*, 47, 3673–3680 (1976).

[Brown, 1978] G.V. Brown, *Practical and efficient magnetic heat pump*, *NASA Tech. Briefs*, 3, 190–191 (1978).

[Brück, 2005] E. Brück, *Developments in magnetocaloric refrigeration*, *Journal of Applied Physics*, 38, 381–391 (2005).

[Cheng, 2014] Ye Cheng, *Thermal behavior of lattice parameter in compounds of the series  $Mn_{5-x}Fe_xSi_3$* , Bachelor thesis, Jülich Centre for Neutron Science, JCNS-2, Peter Gruenberg Institute, PGI-4 (2014).

[Cullity and Stock, 1956] B.D. Cullity, S.R. Stock, *Elements of X-ray diffraction* (1956).

[Czochralski, 1918] J. Czochralski, *A new method for the measurement of the crystallization rate of metals*, *Zeitschrift für Physikalische Chemie*, 92, 219–221 (1918).

[Dan'kov et al., 1997] S.Y. Dan'kov, A.M. Tishin, V.K. Pecharsky, K.A. Gschneidner Jr., *Experimental device for studying the magnetocaloric effect in pulse magnetic fields*, *Review of Scientific Instruments*, 68, 2432 (1997).

[Dan'kov et al., 1998] S.Y. Dan'kov, A.M. Tishin, V.K. Pecharsky, K.A. Gschneidner Jr., *Magnetic phase transitions and the magnetothermal properties of gadolinium*, *Physical Review B*, 57, 3478 (1998).

[Debye, 1926] P. Debye, *Einige Bemerkungen zur Magnetisierung bei tiefer Temperatur*, *Annalen der Physik*, 81, 1154 (1926).

[Dynacool user's manual] RUL:

[http://www.mrfn.org/sites/www.mrfn.org/files/instrument/DynaCool Manual\\_A0.pdf](http://www.mrfn.org/sites/www.mrfn.org/files/instrument/DynaCool Manual_A0.pdf)

[Foldeaki et al., 1995] M. Foldeaki, R. Chahine, and T.K. Bose, *Magnetic measurements: A powerful tool in magnetic refrigerator design*, *Journal of Applied Physics*, 77, 3528 (1995).

[Fujieda et al., 2002] S. Fujieda, A. Fujita, K. Fukamichi, Large magnetocaloric effect in  $La(Fe_xSi_{1-x})_{13}$  itinerant-electron metamagnetic compounds, Applied Physics Letters, 81, 1276 (2002).

[Giauque, 1927] W.F. Giauque, A thermodynamic Treatment of Certain Magnetic Effects. A proposed Method of Producing Temperatures Considerably Below  $1^\circ$  Absolute, American Chemical Society, 49, 1864-1870 (1927).

[Giauque and MacDougall, 1933] W.F. Giauque and D.P. MacDougall, Attainment of Temperatures Below  $1^\circ$  Absolute by Demagnetization of  $Gd_2(SO_4)_3 \cdot 8H_2O$ , Physical Review, 43, 768 (1933).

[Gopal et al., 1997] B.R. Gopal, R. Chahine, and T. K. Bose, A sample translatory type insert for automated magnetocaloric effect measurements, Review of Scientific Instruments, 68, 1818 (1997).

[Gourdon et al., 2014] O. Gourdon, M. Gottschlich, J. Persson, C. de la Cruz, V. Petricek, M. A. McGuire, T. Bruckel, Toward a better understanding of the magnetocaloric effect: An experimental and theoretical study of  $MnFe_4Si_3$ , Journal of Solid State Chemistry, 216, 56–64 (2014).

[Green et al., 1990] G. Green, J. Chafe, J. Stevens, J. Humphrey, A gadolinium terbium active regenerator, Advances in Cryogenic Engineering, 35, 1165–1174 (1990).

[Gschneidner et al., 2005] K.A. Gschneidner Jr., V.K. Pecharsky and A.O. Tsokol, Recent developments in magnetocaloric materials, Reports On Progress In Physics, 68, 1479–1539 (2005).

[Gschneidner et al., 2008] K.A. Gschneidner, Jr., V.K. Pecharsky, Thirty years of near room temperature magnetic cooling: Where we are today and future prospects, International Journal of Refrigeration, 31, 945 – 961 (2008).

[Gschneidner et al., 2012] K.A. Gschneidner Jr., Y. Mudryk, V.K. Pecharsky, On the nature of the magnetocaloric effect of the first-order magnetostructural transition, Scripta Materialia 67 572–577 (2012).

[Hansen, 2010] B. R. Hansen, Materials for Room Temperature Magnetic Refrigeration, Ph.D. thesis, Technical University of Denmark (2010).

[Hering et al., 2015] P. Hering, K. Friese, J. Voigt, J. Persson, N. Aliouane, A. Grzechnik, A. Senyshyn, T. Brückel, Structure, Magnetism, and the Magnetocaloric Effect of  $MnFe_4Si_3$  Single Crystals and Powder Samples, Chemistry of Materials, 27, 7128-7136 (2015).

[Johnson et al., 1972] V. Johnson , J.F. Weiher, C.G. Frederick, D.B. Rogers, Magnetic and Mössbauer effect studies of Mn<sub>5</sub>Si<sub>3</sub>:Fe<sub>5</sub>Si<sub>3</sub> solid solutions, Journal of Solid State Chemistry, 4,311-323 (1972).

[Kuz'min, 2007] M.D. Kuz'mina, Factors limiting the operation frequency of magnetic refrigerators, Applied Physics Letters, 90, 251916 (2007).

[Le Bail et al., 1988] D.H. Le Bail, A. and J. L. Fourquet, Ab-initio structure determination of LiSbWO<sub>6</sub> by X-Ray powder diffraction, Materials Research Bulletin, 23, 447-452 (1988).

[Morrish, 1965] A.H. Morrish, The Physical Principles of Magnetism, Wiley, New York, Chapter 3 (1965).

[Oliveira and Ranke, 2010] N.A. de Oliveira and P.J. Ranke, Theoretical aspects of the magnetocaloric effect, Physics Report, 89-159 (2010).

[Pecharsky and Gschneidner Jr, 1997] V.K. Pecharsky and K.A. Gschneidner Jr., Giant Magnetocaloric Effect in Gd<sub>5</sub>(Si<sub>2</sub>Ge<sub>2</sub>), Physical Review Letters, 78, 4494 (1997).

[Pecharsky and Gschneidner Jr, 1999] V.K. Pecharsky and K.A. Gschneidner Jr., Magnetic refrigeration material, Journal of Applied Physics, 85, 5365 (1999).

[Petricek et al., 2006] V. Petricek, M. Dusek, L. Palatinus, Jana 2006 Crystallographic computing system for standard and modulated structures, Version 30/11/2014 (2006).

[Skourski et al., 2011] Y. Skourski, M.D. Kuz'min, K.P. Skokov, A.V. Andreev, and J. Wosnitza, High-field magnetization of Ho<sub>2</sub>Fe<sub>17</sub>, Physical Review, B 83, 214420 (2011).

[Songlin et al., 2002] Songlin, Dagula, O. Tegus, E. Bruck, J.C.P. Klaasse, F.R. de Br, and K.H. J. Buschow, Magnetic phase transition and magnetocaloric effect in Mn<sub>5-x</sub>Fe<sub>x</sub>Si<sub>3</sub>, Journal of Alloys and Compounds, 334, 249–252 (2002).

[Stefanovsky et al., 2016] S.V. Stefanovsky, S.V. Yudintsev, S.E. Vinokurov and, B.F. Myasoedov, Chemical-Technological and Mineralogical-Geochemical Aspects of the Radioactive Waste Management, Geochemistry International (2016).

[Tegus et al., 2002] O. Tegus, E. Brueck, K.H.J. Buschow and F.R. de Boer, Transition-metal-based magnetic refrigerants for room-temperature, Nature, 415, 150-152 (2002).

#### [WEB OF SCIENCE](#)

<http://en.wikipedia.org>

[Yu et al., 2003] B.F. Yu, Q. Gao, B. Zhang, X.Z. Meng, Z. Chen, Review on research of room temperature magnetic refrigeration, International Journal of Refrigeration, 26, 622 – 636 (2003).

[Zavareh, 2016] M. Ghorbani-Zavareh, *Direct Measurements of the Magnetocaloric Effect in Pulsed Magnetic Fields*, PhD thesis, Helmholtz Center Dresden-Rossendorf, Institute of High-Magnetics Dresden, Faculty of Mathematics and Natural Sciences, The Technical University of Dresden (2016).

[Zherlitsyn et al., 2012] S. Zherlitsyn, B. Wustmann, T. Herrmannsdörfer, and J. Wosnitza, *Status of the Pulsed-Magnet-Development Program at the Dresden High Magnetic Field Laborator*, IEEE Transactions, Applied Superconductivity, 22, 4300603 (2012).

[Zimmet. al., 1998] C.B. Zimm, A. Jastrab, A. Sternberg, V. Pecharsky, K. Geschneidner Jr., M. Osborne and I. Anderson, *Description and Performance of a Near-Room Temperature Magnetic Refrigerator*, Advances in Cryogenic Engineering,43 (1998).

## Appendix A

- Set Temperature 30K at 5K/min. No O'Shoot
- Wait For Temperature, Delay 60 secs (1.0 mins), No Action
- New Datafile "C:\QdDynacool\Data\Nour\MnFe4Si3\_30K\_MvsB.dat"
- VSM Moment vs Field 4 Quadrants -10000 Oe to 10000 Oe Sweep Continuous Auto Center ON
- Set Temperature 40K at 5K/min. No O'Shoot
- Wait For Temperature, Delay 60 secs (1.0 mins), No Action
- New Datafile "C:\QdDynacool\Data\Nour\MnFe4Si3\_40K\_MvsB.dat"
- VSM Moment vs Field 4 Quadrants -10000 Oe to 10000 Oe Sweep Continuous Auto Center ON

**Figure A1: Part of the command sequence used in the magnetization measurements with  $H \parallel a$ -axis which was performed on PPMS-Dynacool.**

- Set Magnetic Field 60000.0Oe at 200.0Oe/sec, Linear, Persistent
- Set Temperature 60K at 5K/min. No O'Shoot
- Wait For Temperature, Field, Delay 60 secs, No Action
- New Datafile "C:\Messdaten\Data\Maraytta\repeate\_lastmeasurements\60K.dat"
- VSM Moment vs Field 1 Quadrant 60000 Oe to 5000 Oe Sweep Continuous Auto Center ON
- VSM Moment vs Field 1 Quadrant 5000 Oe to 80000 Oe Sweep Continuous Auto Center ON
- Set Magnetic Field 60000.0Oe at 200.0Oe/sec, Linear, Persistent
- Set Temperature 80K at 5K/min. No O'Shoot
- Wait For Temperature, Field, Delay 60 secs, No Action
- New Datafile "C:\Messdaten\Data\Maraytta\repeate\_lastmeasurements\80K.dat"
- VSM Moment vs Field 1 Quadrant 60000 Oe to 5000 Oe Sweep Continuous Auto Center ON
- VSM Moment vs Field 1 Quadrant 5000 Oe to 60000 Oe Sweep Continuous Auto Center ON

**Figure A2: Parts of the command sequence used in the last magnetization measurements in the direction ( $H \parallel c$ -axis) which were performed on the PPMS.**

```

plt.plot(temp_measured,moment[:,[589]],label="5.89T")
plt.plot(temp_measured,moment[:,[500]],label="5.00T")
plt.plot(temp_measured,moment[:,[450]],label="4.50T")
plt.plot(temp_measured,moment[:,[400]],label="4.00T")
plt.plot(temp_measured,moment[:,[350]],label="3.50T")
plt.plot(temp_measured,moment[:,[300]],label="3.00T")
plt.plot(temp_measured,moment[:,[250]],label="2.5T")
plt.plot(temp_measured,moment[:,[200]],label="2.00T")
plt.plot(temp_measured,moment[:,[150]],label="1.5T")
plt.plot(temp_measured,moment[:,[100]],label="1.00T")
plt.plot(temp_measured,moment[:,[50]],label=".50T")
plt.plot(temp_measured,moment[:,[1]],label=".01T")
plt.legend(loc="upper left", bbox_to_anchor=[1, 1], ncol=1, shadow=None, title="Field", fancybox=True)
xlabel ('Temperature (K)')
ylabel('Magnetization (A m^2/kg)')
plt.savefig('ime.png', dpi=400,bbox_inches='tight')

```

```

plt.plot(temp_measured,moment[:,[90]],label="0.9T")
plt.plot(temp_measured,moment[:,[70]],label="0.7T")
plt.plot(temp_measured,moment[:,[50]],label="0.5T")
plt.plot(temp_measured,moment[:,[30]],label="0.3T")
plt.plot(temp_measured,moment[:,[20]],label="0.2T")
plt.plot(temp_measured,moment[:,[18]],label="0.18T")
plt.plot(temp_measured,moment[:,[10]],label="0.1T")
plt.plot(temp_measured,moment[:,[5]],label="0.05T")
plt.plot(temp_measured,moment[:,[1]],label="0.01T")
plt.legend(loc="upper left", bbox_to_anchor=[1, 1], ncol=1, shadow=None, title="Field", fancybox=True)
xlabel ('Temperature (K)')
ylabel('Magnetization (Am^2/kg)')
plt.savefig('ime.png', dpi=400,bbox_inches='tight')

```

**Figure A3: Python scripts which were used to plot the temperature-dependent magnetization curves of  $\text{MnFe}_4\text{Si}_3$  in  $\mathbf{H} \parallel [100]$  and  $\mathbf{H} \parallel [001]$  respectively.**

## القياس المباشر لظاهر التبريد المغناطيسي في مركبات السلسلة $Mn_{5-x}Fe_xSi_3$

إعداد: نور عبد المجيد محمد مرايطة

إشراف: د. سلمان محمد سلمان ود. كارين فريزي

### ملخص:

تم في هذا البحث تحضير عينة بلورية مفردة من المركب  $MnFe_4Si_3$  وتنقيح البنية البلورية للعينة على درجة حرارة الغرفة عن طريق استخدام حيود الأشعة السينية المنعكسة عن مسحوق المركب. وقد أكدت النتائج أن البلورة لا تحتوي على أي شوائب .

تم دراسة السلوك المغناطيسي وظاهرة التبريد المغناطيسي للعينة, حيث تم قياسهما في مجال مغناطيسي ثابت ومتردد. وقد تم إجراء القياسات بحيث كان المجال موازي للاتجاه [100] في المرة الأولى , ثم مرة أخرى حيث المجال موازي للاتجاه [001]. وقد أكدت النتائج التي حصلنا عليها من قياسات المغناطيسية باستخدام جهاز PPMS وجهاز PPMS Dynacool على تباين المغنطة للمادة باختلاف اتجاه المجال المغناطيسي مع وقوع الاتجاه المفضل للمغنطة في المستوى a,b. كما أكدت أيضا على اعتماد قيم المغنطة على قيمة المجال المغناطيسي وعلى أن درجة حرارة التحول للفيرومغناطيسية هي 300 كلفن وهذا ما تم تأكيده في دراسات سابقة.

تم استخدام قوانين ماكسويل لحساب التغير في الإنتروبي والذي يعتبر مقياس لظاهرة التبريد المغناطيسي في المادة. وقد وجد أنها الأكبر في الاتجاه التفضيلي للتمغنط ([100]). وبشكل عام كانت القيم أقل من التي رصدت في دراسات سابقة. كما تم قياس المغنطة للعينة في مجال مغناطيسي متردد وأظهرت النتائج توافقا كبيرا مع النتائج التي حصلنا عليها في المجال المغناطيسي الثابت.

في النهاية تم دراسة ظاهرة التبريد المغناطيسي للعينة عن طريق القياس المباشر للتغير الأدياباتيك في درجة الحرارة في مجال مغناطيسي متردد يصل إلى 50 تسلا ووجد أن الظاهرة تعتمد على قيمة المجال المغناطيسي. وكانت القيمة العظمى بتغير 1.3 كلفن في مجال متردد بقيمة 2 تسلا و 5.66 كلفن في مجال 20 تسلا .